Supporting Information

Unlocking the Potential of Antisolvent-Free Perovskite Solar Cells: Modulating Crystallization and Intermediates through a Binary Volatile Additive Strategy

Bo Zhou[a], Pei Zhao[b], Junxue Guo[a,c], Yu Qiao[a], Shuaifeng Hu[d], Xin Guo[a], Jiewei Liu[a,*], Can Li[a,c,*]

[a] *State Key Laboratory of Catalysis, Dalian National Laboratory for Clean Energy, Dalian Institute of Chemical Physics, Chinese Academy of Sciences, Dalian 116023, China*

[b] *Research Center for Computational Science, Institute for Molecular Science, Okazaki 444-8585, Japan*

[c] *School of Chemistry and Materials Science, University of Science and Technology of China, Hefei 230026, China*

[d] *Clarendon Laboratory, Department of Physics, University of Oxford, Parks Road, Oxford OX1 3PU, U.K.*

* Corresponding author.

E-mail addresses: jwliu@dicp.ac.cn (J. Liu), canli@dicp.ac.cn (C. Li)

Keywords:

Binary volatile additives; Crystallization window; Intermediates; Perovskite solar cells; Antisolvent-free

Experimental Section

Materials:

Anhydrous N-methyl-2-pyrrolidone (NMP, 99.9%), and N,N-dimethylformamide (DMF, 99.8%) were purchased from Sigma-Aldrich. SnO_2 colloid precursor (tin (IV) oxide, 15% in H2O colloidal dispersion) was purchased from Alfa Asear. Formamidinium iodide (FAI), cesium iodide (CsI), lead chloride ($PbCl_2$), lead iodide (PbI_2), methylammonium chloride (MACl), 2,2',7,7'-Tetrakis (N,N-di-pmethoxyphenylamine)-9,9'spirobifluorene (Spiro-OMeTAD) were purchased from Xi'an Polymer Light Co. Ltd. Trifluoroacetamide (TFAA), 4-tert-butyl pyridine (TBP) and lithium bis(trifluoromethane) sulfonimide (Li-TFSI) were purchased from Shanghai Aladdin Biological Technology Co. Ltd. All these commercially available materials were used without any further purification

Preparation for solutions:

The $(FA_{0.9}Cs_{0.1})PbI_3$ perovskite precursor solution (2 M, contained 10% $PbCl_2$) was prepared by mixing FAI (154.8 mg), CsI (26 mg), $PbCl_2$ (27.8 mg), and PbI_2 (461 mg) in DMF: NMP = 5:1 by volume. The different perovskite precursor solutions were prepared with further addition of different amounts of MACl and TFAA (with molar ratio to perovskite). To prepare the Spiro-OMeTAD solution, 72.3 mg of Spiro-OMeTAD was dissolved in 1 mL of CB, which contained 29 μL of TBP and 17.5 μL of LiTFSI (520 mg/mL).

Device fabrication:

The ITO-coated glass substrate was ultrasound in deionized water, ethanol, isopropanol, and ethanol for 30 minutes each, respectively. The substrate was then dried with a nitrogen gun and treated with ultraviolet ozone for 30 minutes. The SnO_2 precursor solution (1:4 volume ratio of SnO2 colloidal solution to deionized water) was spin-coated on the ITO glass at 4000 rpm for 30 s, and the corresponding SnO_2 film was annealed at 150°C for 30 minutes. Prior to spin-coating, the substrate was treated with ultraviolet ozone for 20 minutes to improve wettability and then transferred to a glove box. For the perovskite film, 70 μL of the precursor solution was spin-coated in one step onto the substrate at 5000 rpm for 60 s with 2500 rpm s^{-1} without antisolvent. The film was dried on a hot plate at 100 °C for 10 minutes and subsequently annealed at 150 °C for 15 minutes. After cooling to room temperature, 35 μL of the Spiro-OMeTAD solution was spin-coated at 3500 rpm for 30 seconds to form the HTL. Finally, approximately 100 nm of Au was thermally deposited on the Spiro-OMeTAD layer under a pressure of 7×10^{-4} Pa, and the devices were oxidized for 24 hours. The active area of each device was 0.04 cm^2.

Material characterizations:

Optical microscopy observations of the evolution of wet films based on various perovskite precursors were conducted using an optical microscope equipped with a camera and computer (Olympus). The dynamic light scattering (DLS) spectra of the perovskite precursor solutions were acquired by ZetaSizer Nano. The ultraviolet-visible (UV-Vis) spectra of the perovskite films were collected using a UV-2600 spectrophotometer. In situ UV-Vis absorption spectroscopy was performed using the Lambda950 spectrometer, with a measurement range of 400-800 nm and a sampling time of 5 seconds. Ultraviolet photoelectron spectroscopy (UPS) measurements were taken using the Thermo ESCALAB 250XI. X-ray diffraction (XRD) patterns of perovskite films were obtained using the Smartlab with a scan rate of 20°/ min. Grazing-Incidence Wide-Angle X-Ray Scattering (GIWAXS) data were collected at the Beamline BL14B1 at the Shanghai Synchrotron Radiation Facility (SSRF) using an incident photon energy of 10 keV (wavelength of 1.2398 Å) based on different incident angles and an exposure time of 30 seconds. Scanning electron microscopy (SEM) images and Energy-dispersive spectroscopy (EDS) of the films were captured using the JSM-7800F SEM instrument with an acceleration voltage of 3 kV. Fourier transform infrared (FTIR) spectroscopy was performed using the FTIR-Nicolet iS50 (4000 to 500 cm^{-1}). Thermogravimetry-mass spectra (TG-MS) were measured using a Diamond TG/DTA instrument. The 1H NMR and 19F NMR spectra were acquired on an AVANCE III HD 700MHz spectrometer. Raman spectra were recorded using the Horiba LabRAM HR Evolution Spectroscope. X-ray photoelectron spectroscopy (XPS) was performed on perovskite films to analyze binding energy and element composition, and a monochromatized Al Kα source was used (Thermo escalab 250Xi). Photoluminescence (PL) spectra and time-resolved photoluminescence (TRPL) decay spectra were recorded using the fluorescence spectrophotometer and fluorescence lifetime system (FLSP920) spectrometer, respectively. PL mapping was performed using a PL microscopic spectrometer (FV1000MPE) with mapping capability. Atomic Force Microscopy (AFM) and Kelvin Probe Force Microscopy (KPFM) were carried out on a Bruker Dimension ICON.

Device characterizations:

Photovoltaic performance measurements were conducted under 1sun intensity (100 mW/cm^2) using a xenon-lamp-based solar simulator (3A, Enli Tech). The intensity of the solar spectrum was calibrated using a monocrystalline silicon solar cell (Enli Tech.). The *J-V* characteristics were performed with forward and reverse scans between -0.1 to 1.2 V, with a voltage step of 0.02 V and delay time of 2 ms, using a Keithley 2400 source meter (Keithley Instrument). Electrical impedance spectroscopy (EIS) plotting of all devices was carried out with a

frequency range from 10^6 Hz to 1 Hz on the Zahner electrochemical workstation. The external quantum efficiency (EQE) measurements were conducted on a solar-cell spectral-response measurement system (QE-R, Enli tech). The slope n (ideal factor) by V_{OC} versus light intensity curves is calculated using following equation:

$$n = \frac{q}{k_B T} \frac{V_{oc}}{lnW}$$

where k_B, q, V_{OC}, and W represented the Boltzmann constant, elementary charge, open-circuit voltage, and light intensity, respectively. The space-charge limited current (SCLC) measurements were performed using hole-only devices with a structure of ITO/PTAA/perovskite/Spiro-OMeTAD/Au under dark conditions. Accordingly, the trap density (N_t) was calculated using the onset voltage of TFL (V_{TFL}) with the formula:

$$N_t = \frac{2 \varepsilon_r \varepsilon_0 V_{TFL}}{q L^2}$$

where ε_r, q, L, and ε_0 represented the dielectric constant, elementary charge, thickness of the perovskite films, and the vacuum permittivity, respectively. The steady-state current density curve was tested under the bias voltage of the corresponding device's maximum power. For environmental storage testing, the devices were placed in an environmental chamber (DHTHM-27-0-P-SD) at the pre-determined humidity and temperature.

Computational methods:

The molecular electrostatic potentials and dipole moments of TFAA and NMP were computed using density functional theory (B3LYP/6-31G(d,p)) and the Gaussian 09 program. The molecular electrostatic potentials were visualized to show electrostatic charges, where the electron-rich and electron-poor regions were represented by red and blue colors, respectively [1].

Geometry optimizations were performed with the ωB97X-D functional [2] combined with the basis sets of 6-311++G(2d,p) [3-5] for C, H, N, F, S and O atoms and LANL2DZ [6] for Pb and I atoms. Optimized geometries were confirmed as minima by frequency calculations. Interaction energies were calculated using the following equation:

$$\Delta E \int ¿ = E(PbI_2 \cdot small\,molecule) - [E(PbI_2) + E(small\,molecule)] ¿$$

All calculations were conducted using the Gaussian 16 suite of programs [7].

Supplementary Fig. S1-S41 and Tables S1-S7

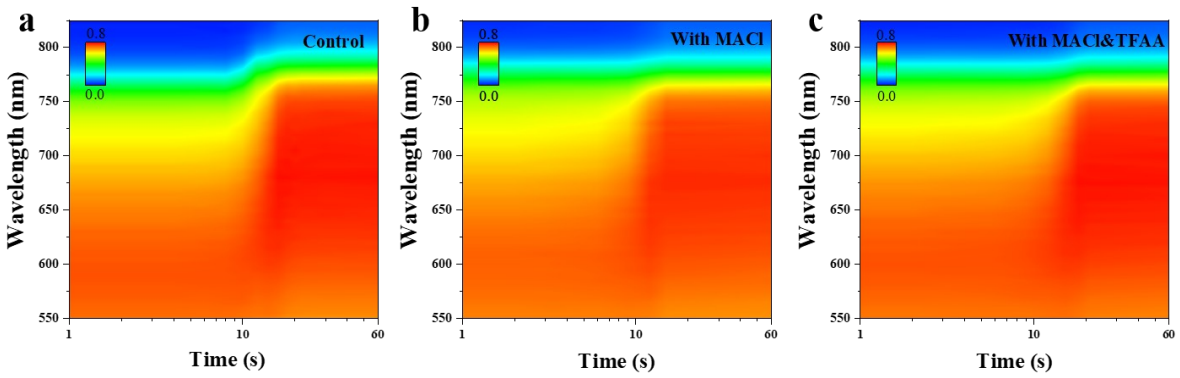

Fig. S1. Contour plot of the film evolution for spin-coating (60s) with different additives: a) Control, b) With MACl, c)With MACl&TFAA. It can be seen that a prolonged spin-coating duration leads to a faster evolution of the perovskite phase during the subsequent annealing, but the change pattern of absorption curve transition is still the same with **Fig. 1a-1c**.

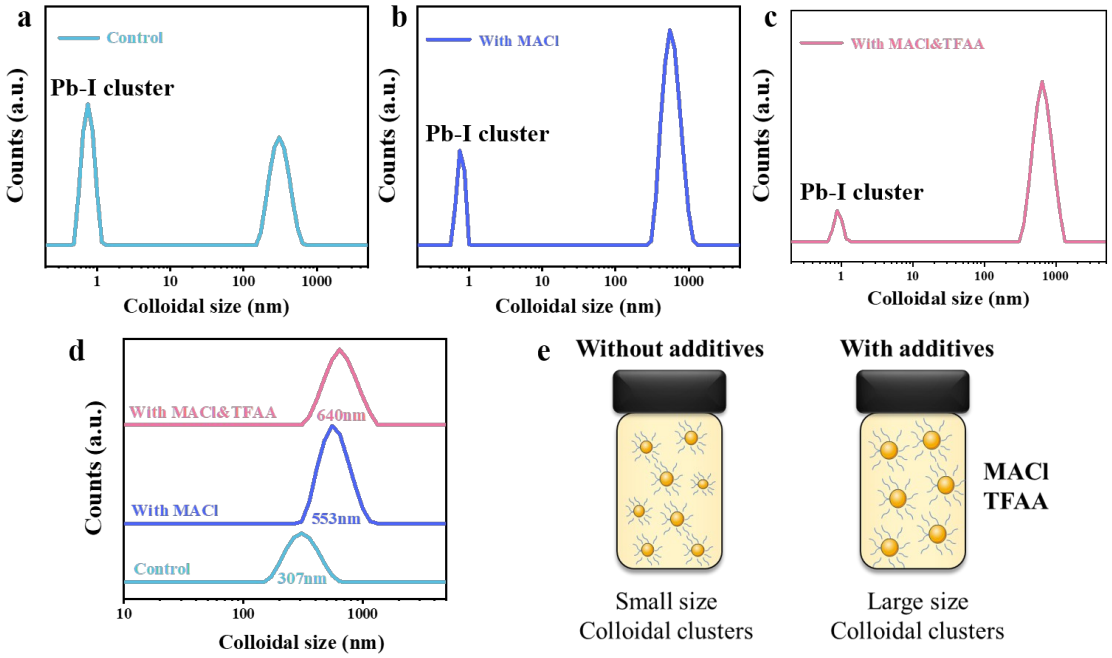

Fig. S2. a-c) DLS spectra of FACs perovskite precursor solutions without or with additives. d) size distributions of different colloidal perovskite precursor solutions measured and e) schematic diagram of colloidal dispersion without or with additives. According to the literature [8], it is known that the first peak in DLS spectra corresponds to the Pb-I cluster

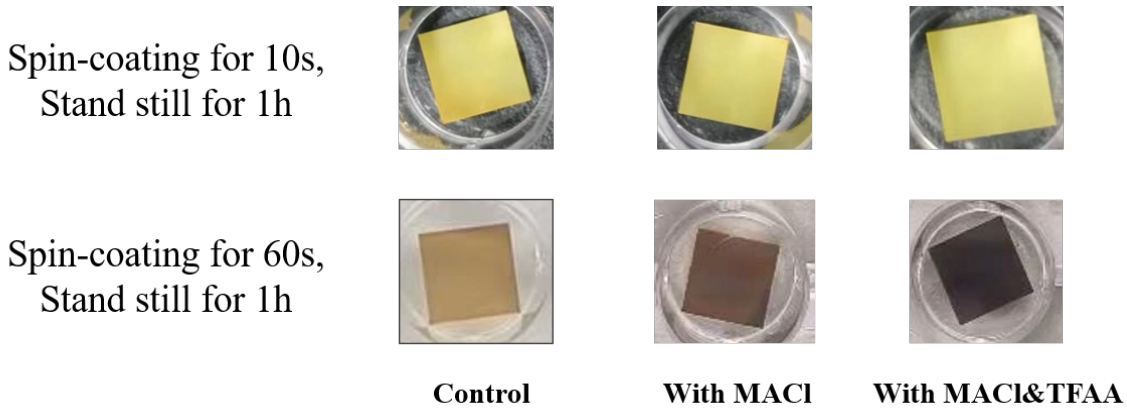

size. It can be observed that the size of Pb-I clusters noticeably decreases upon the addition of additives.

Fig. S3. Photographs of antisolvent-free perovskite films for different spin-coating times in different conditions.

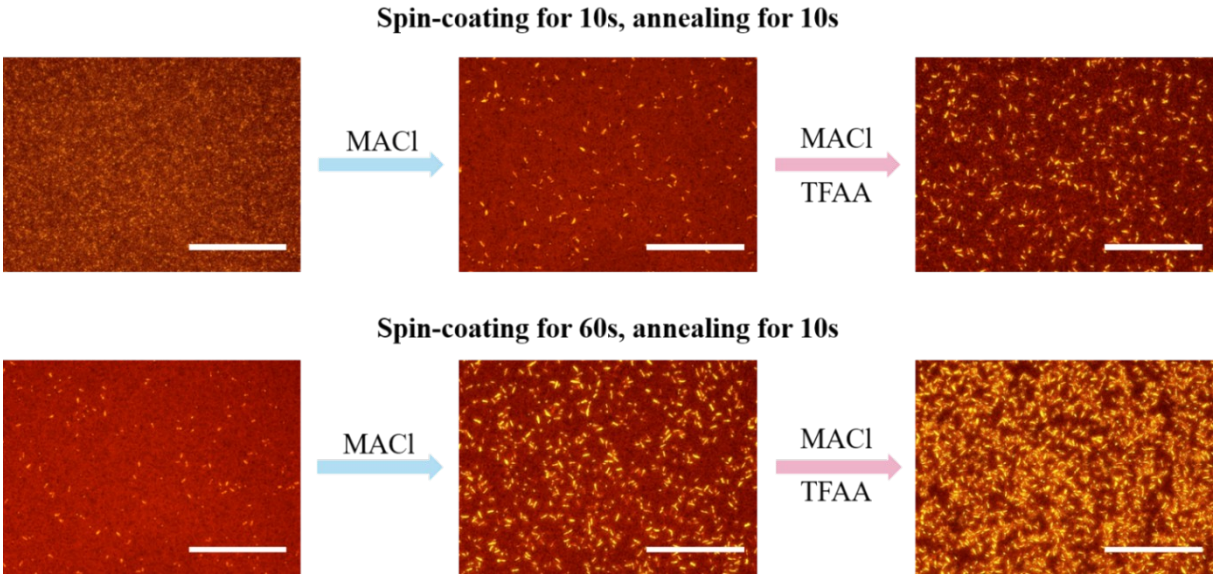

Fig. S4. Optical microscope photographs of perovskite films nucleating from different precursor solutions overlaying PL mapping. Scale bars:100 μm. The yellow portion represents the crystal nuclei, while the red portion corresponds to the wet perovskite films.

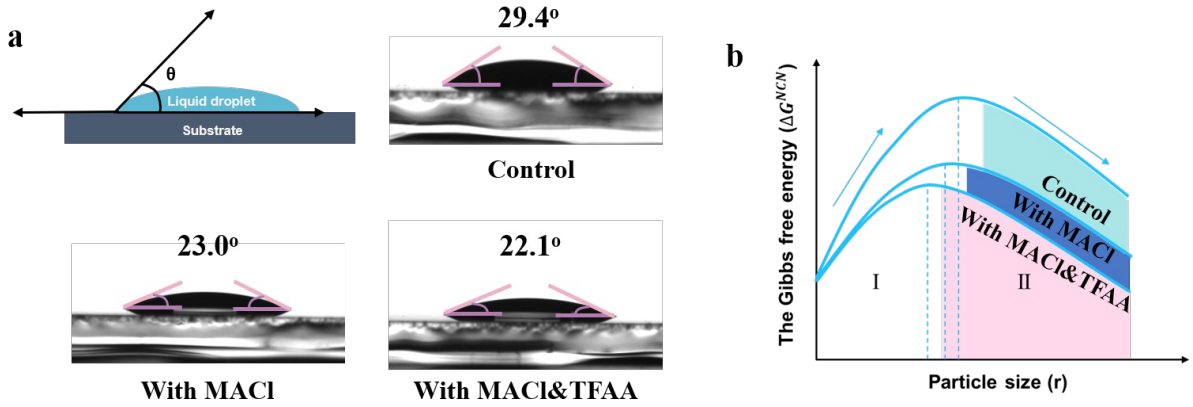

Fig. S5. a) Schematic of droplet equilibrium with the contact angle (θ) on a substrate for non-classical nucleation and contact angles of various solvent mixtures. b) Function relationship between the Gibbs free energy and particle radius.

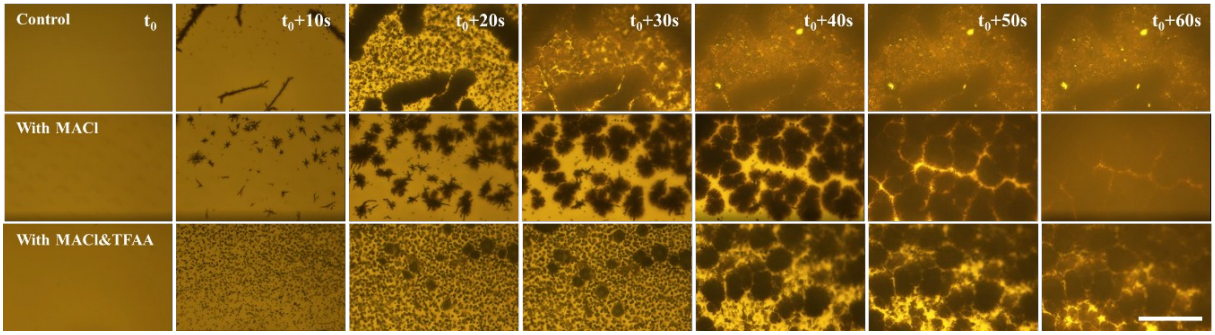

Fig. S6. Observation of different perovskite precursor film morphology evolutions over time with an optical microscope. Scale bars:100 μm.

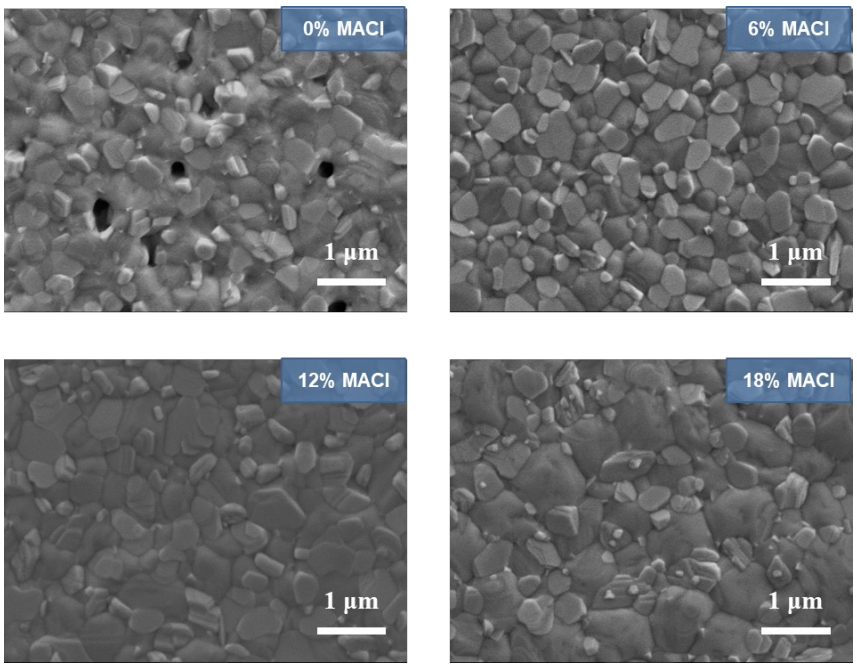

Fig. S7. Top-view SEM images of perovskite films with different concentrations of MACl.

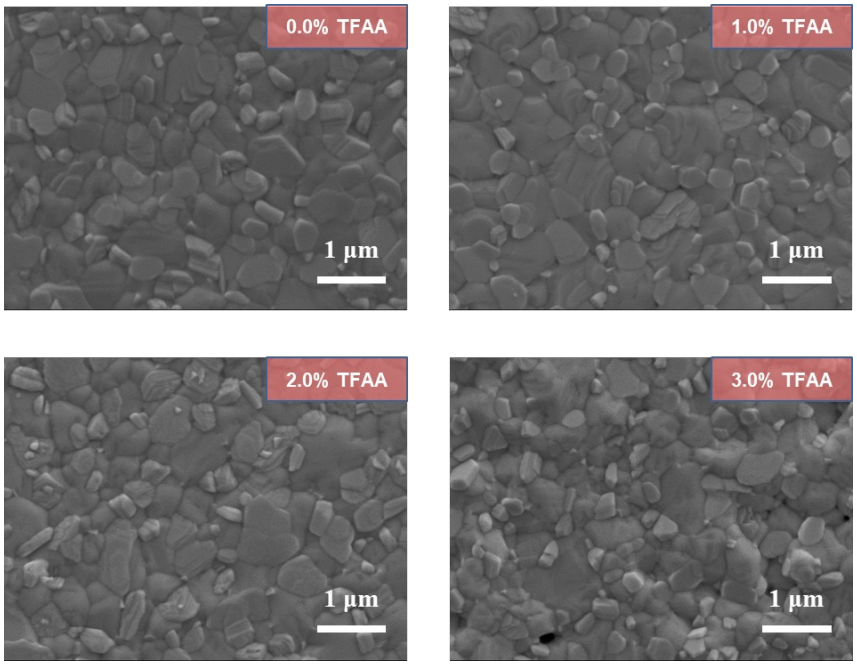

Fig. S8. Top-view SEM images of perovskite films with different concentrations of TFAA.

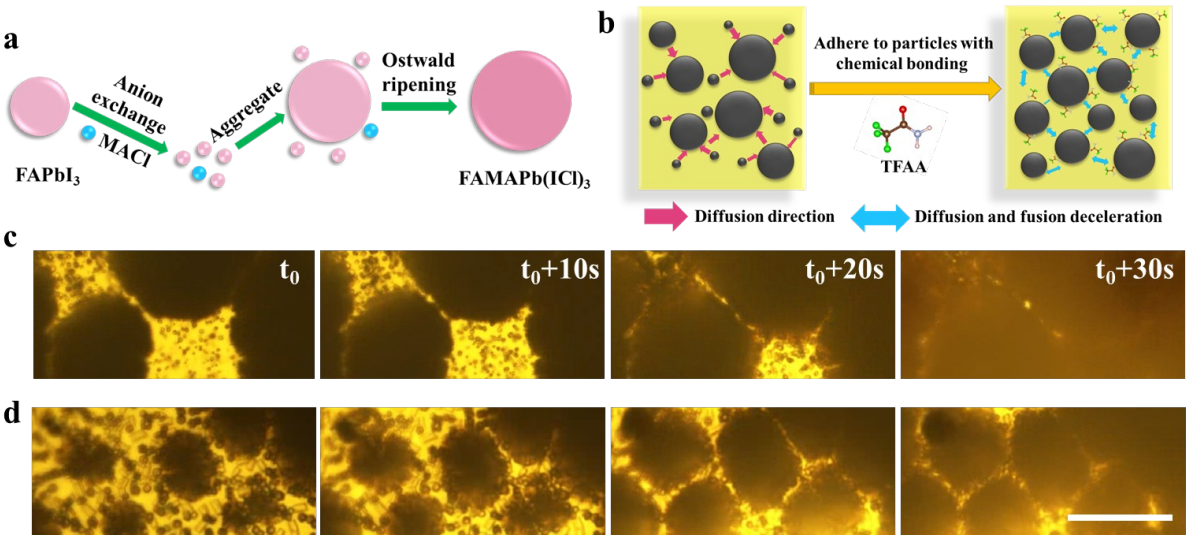

Fig. S9. Scheme of the Ostwald ripening process and their evolutions over time by optical microscope with a,c) MACl or b,d)TFAA-assisted. Scale bars:50 μm.

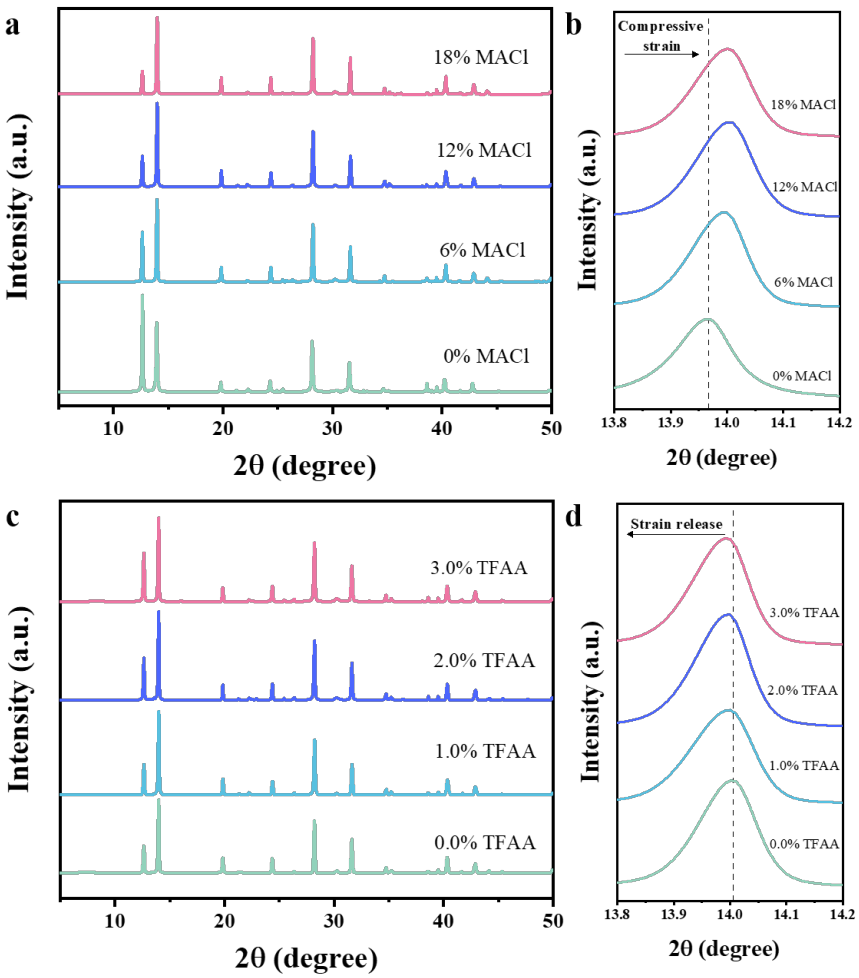

Fig. S10. a,c) XRD patterns of perovskite films with different concentration of additives and b,d) enlarged XRD patterns in the (110) plane position from Fig. S9a and S9c.

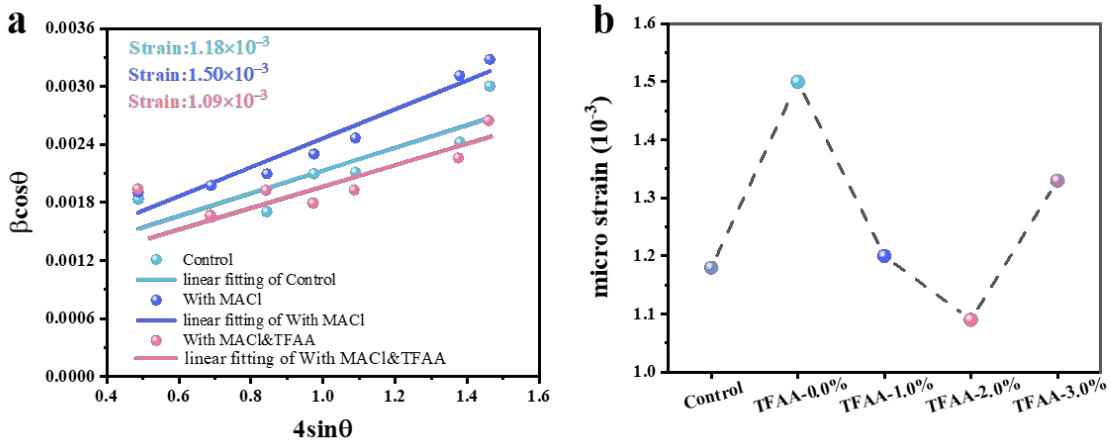

Fig. S11. a) Williamson-Hall plots obtained from XRD patterns of the films with different additives. b) The calculated micro strain variation plot with different amounts of MACl&TFAA.

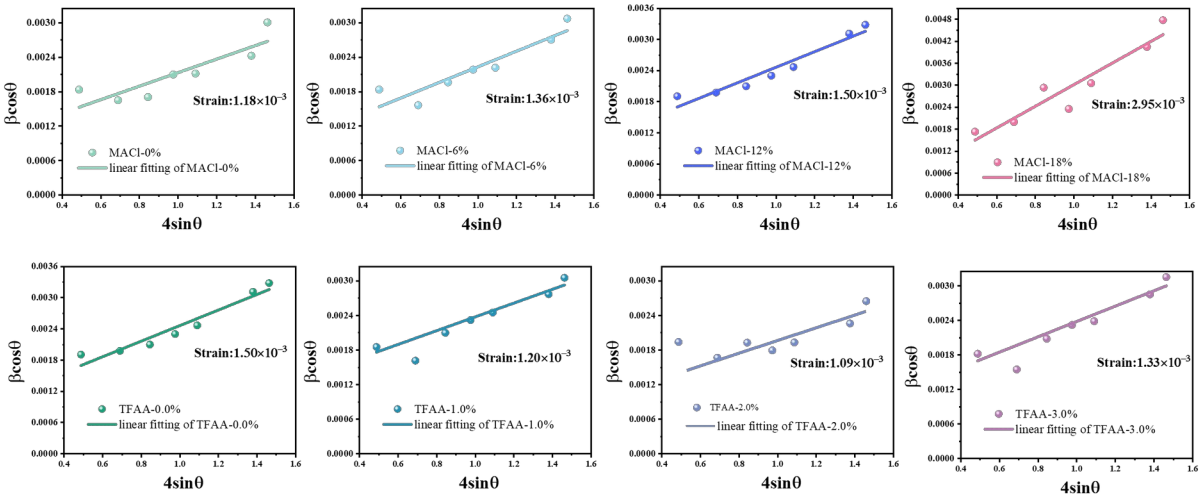

Fig. S12. Williamson-Hall plots from the XRD patterns of the thin films with different amounts of MACl&TFAA.

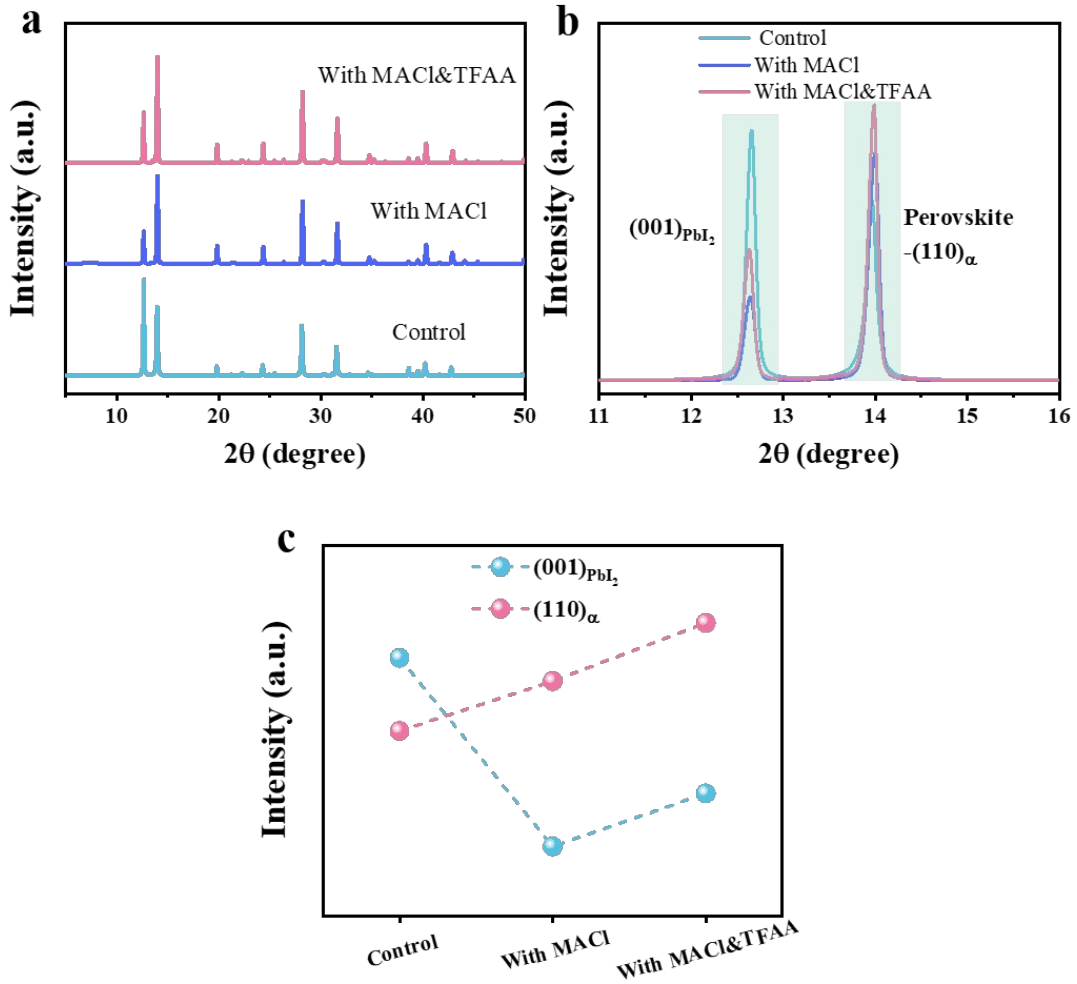

Fig. S13. a) XRD patterns of the films with different additives and b) enlarged XRD patterns about the PbI_2 and (110) plane position from Fig. S12a. c) The calculated intensity variation plots with different additives.

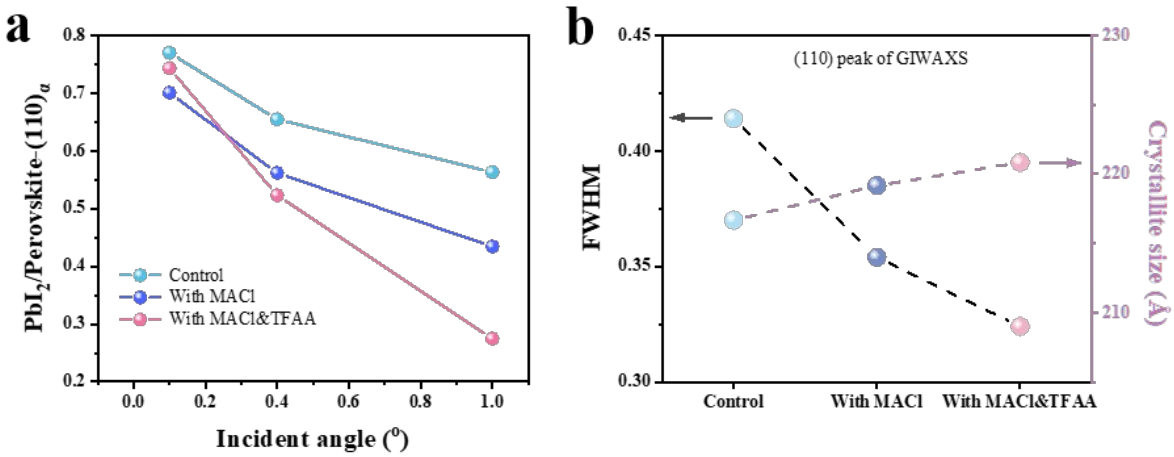

Fig. S14. a) PbI_2/perovskite content ratios as a function of the grazing incident angle for different condition perovskite films. b) The calculated FWHM and crystallite size variation plots with different additives.

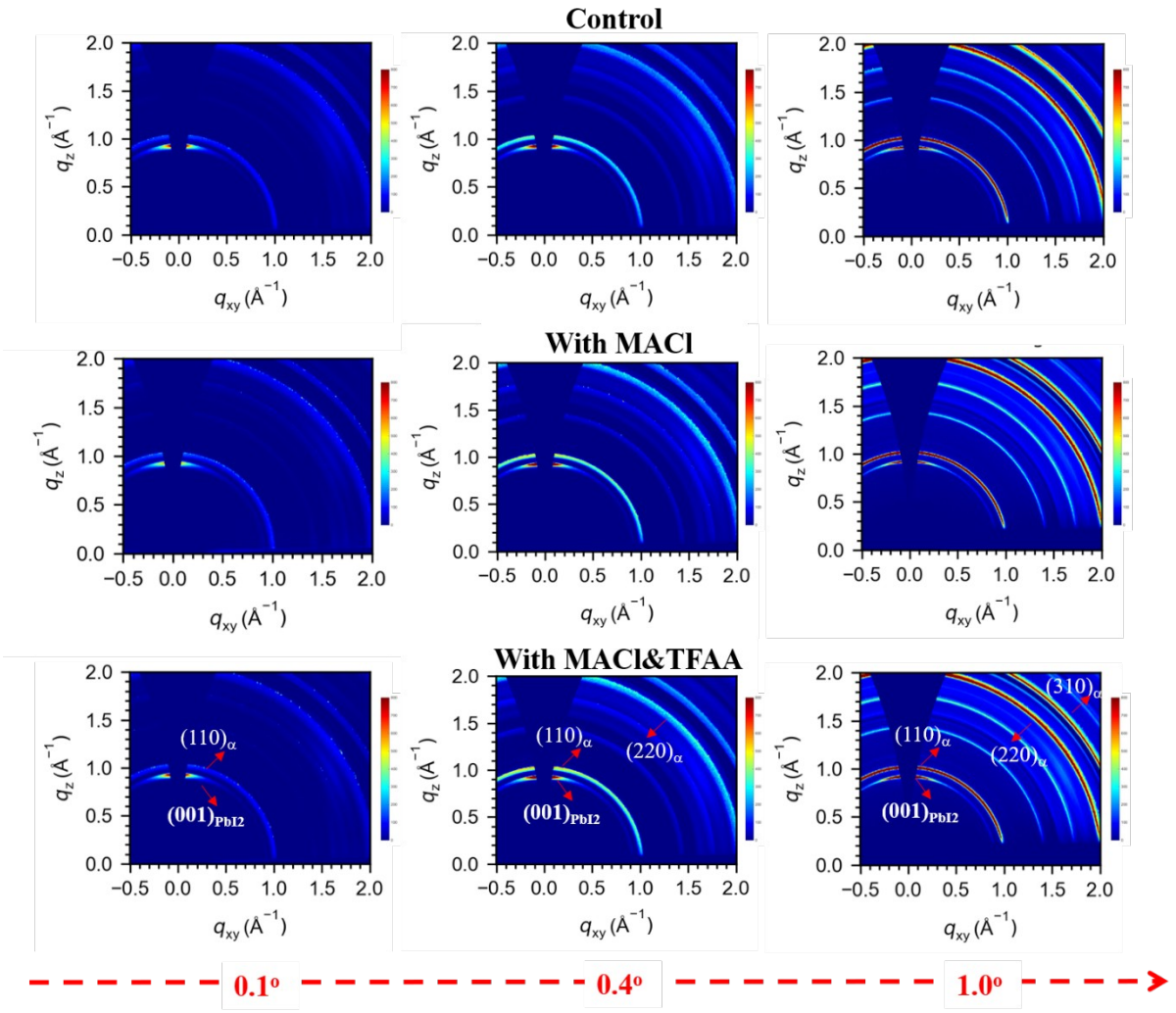

Fig. S15. The GIWAXS of different condition perovskite thin films with different grazing incident angle.

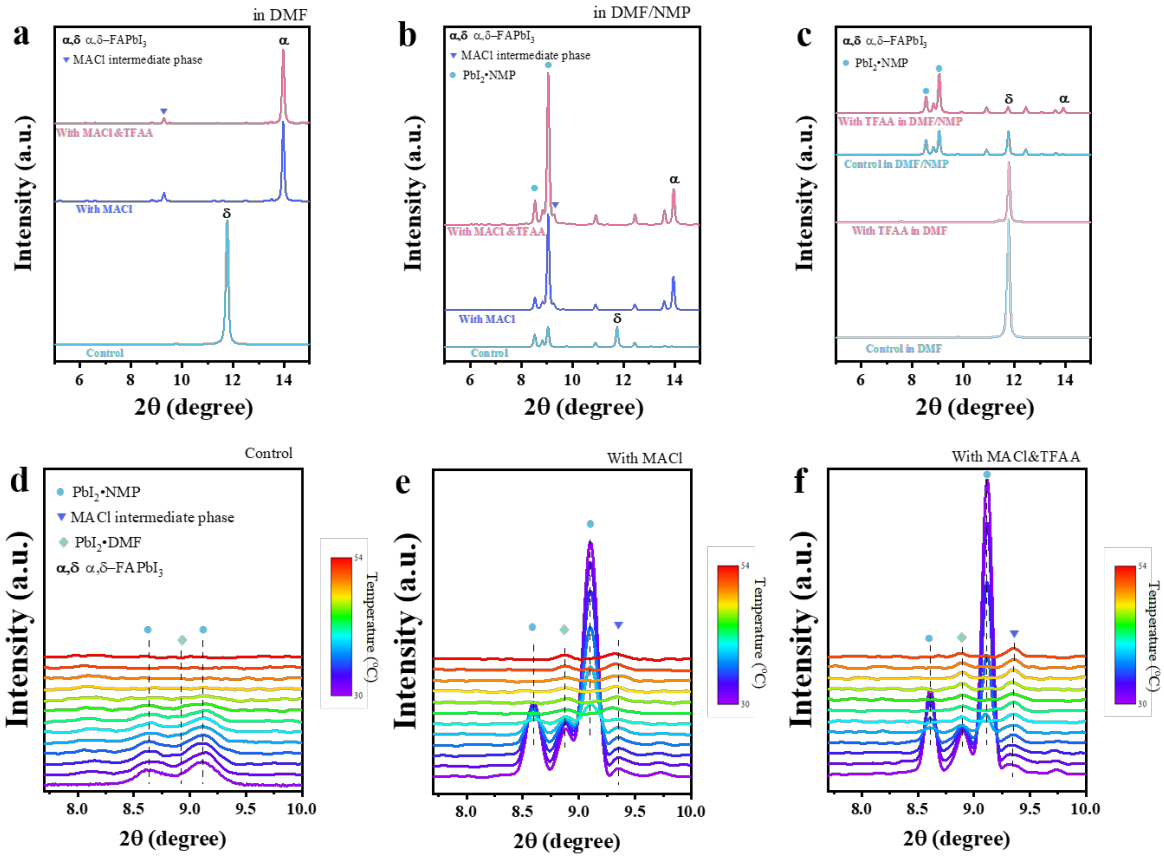
a
in DMF
α,δ α,δ–FAPbI3
MACl intermediate phase
With MACl &TFAA
With MACl
Control
α
δ
Intensity (a.u.)
2θ (degree)
b
in DMF/NMP
α,δ α,δ–FAPbI3
MACl intermediate phase
PbI2•NMP
With MACl &TFAA
With MACl
Control
α
δ
Intensity (a.u.)
2θ (degree)
c
α,δ α,δ–FAPbI3
PbI2•NMP
With TFAA in DMF/NMP
Control in DMF/NMP
With TFAA in DMF
Control in DMF
δ
α
Intensity (a.u.)
2θ (degree)
d
Control
PbI2•NMP
MACl intermediate phase
PbI2•DMF
α,δ α,δ–FAPbI3
Intensity (a.u.)
2θ (degree)
Temperature (°C)
e
With MACl
Intensity (a.u.)
2θ (degree)
Temperature (°C)
f
With MACl&TFAA
Intensity (a.u.)
2θ (degree)
Temperature (°C)

Fig. S16. a-c) XRD patterns of different condition perovskite thin films measured throughout the crystallization process at room temperature. Each XRD patterns were measured after spin coating the precursor solution without annealing. d-f) Enlarged in-situ XRD patterns in the intermediate position from **Fig. 3a**.

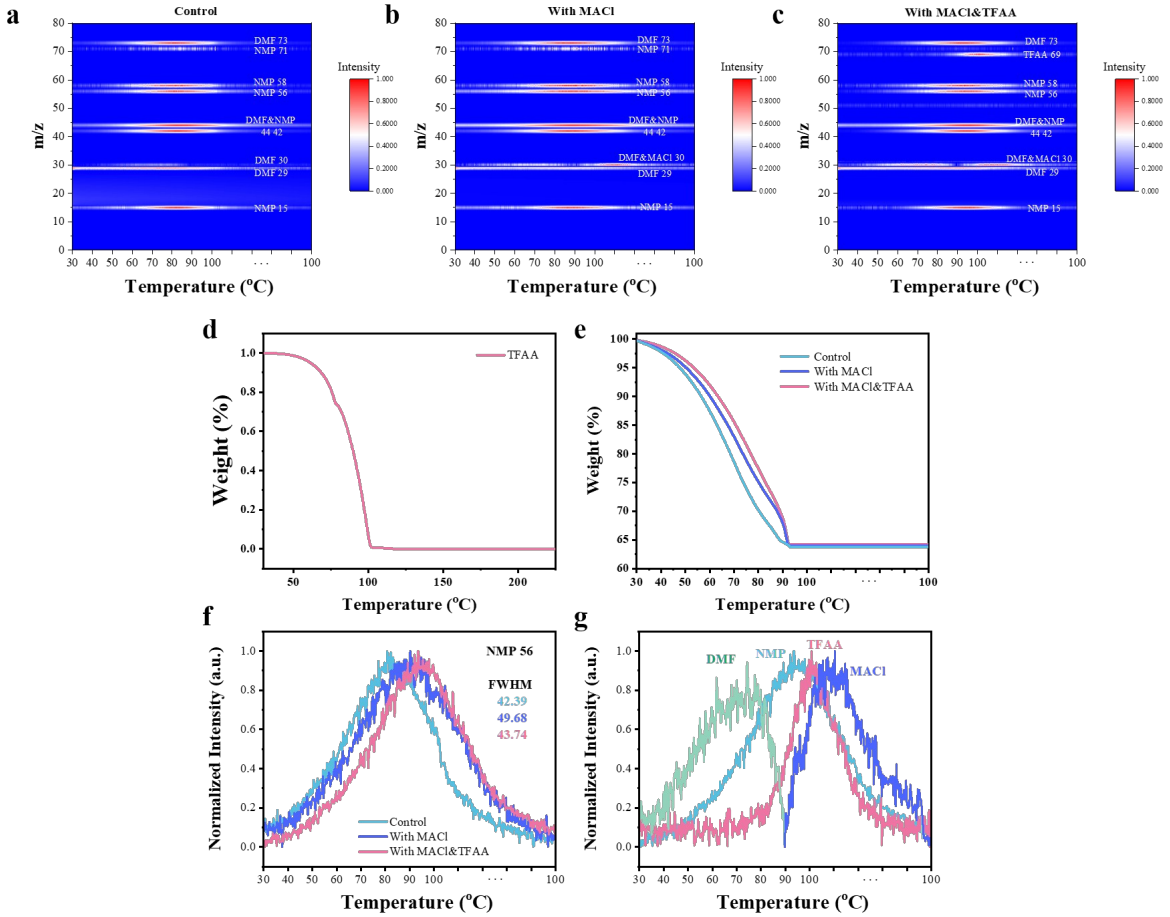

Fig. S17. a-c) TG-MS spectra of perovskite precursor solutions based on different conditions. d-e) TG curves of TFAA powder and precursor solutions based on different conditions. f) Normalized intensity and FWHM variation of NMP extracted from Fig. S16a-S16c. g) Evaporation sequence of DMF&NMP solvent and MACl&TFAA additives. The temperature difference between TG curves and TG-MS spectra is due to the difference in heat transfer. The variation of FWHM reveal that TFAA facilitates the volatile evaporation of NMP via interactions, thereby promoting the transformation of the PbI_2•NMP adduct into dense α-phase perovskite films.

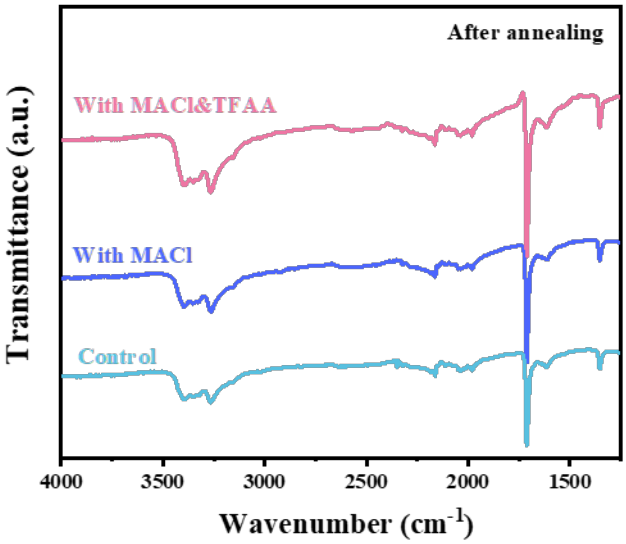

Fig. S18. FTIR spectra of different condition perovskite thin films after annealing. The absence of additional peaks confirms the complete departure of the additives.

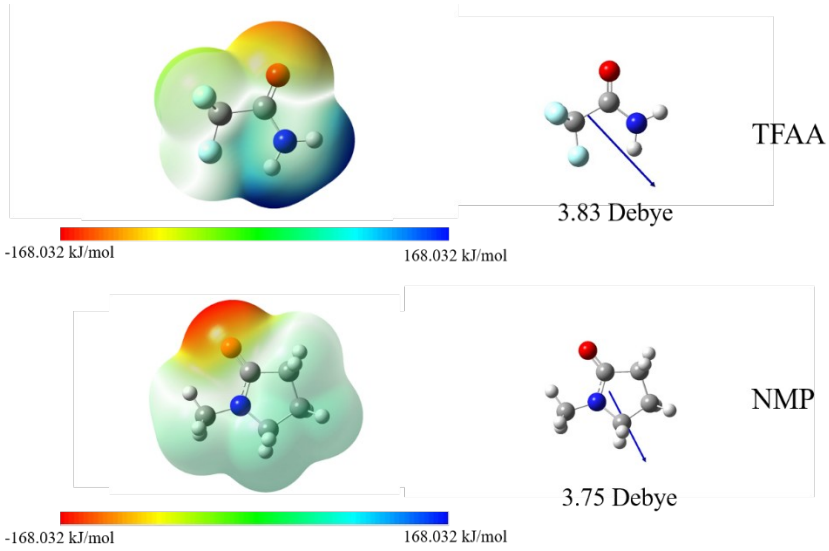

Fig. S19. Molecular electrostatic potentials (ESP) and dipole moments of TFAA and NMP.

Fig. S20. Photo of the perovskite precursor solution with MACl (left, in NMP, ~20 mg ml^{-1}), and the precursor solution with a mixture of the TFAA (right, in NMP, ~20 mg ml^{-1}).

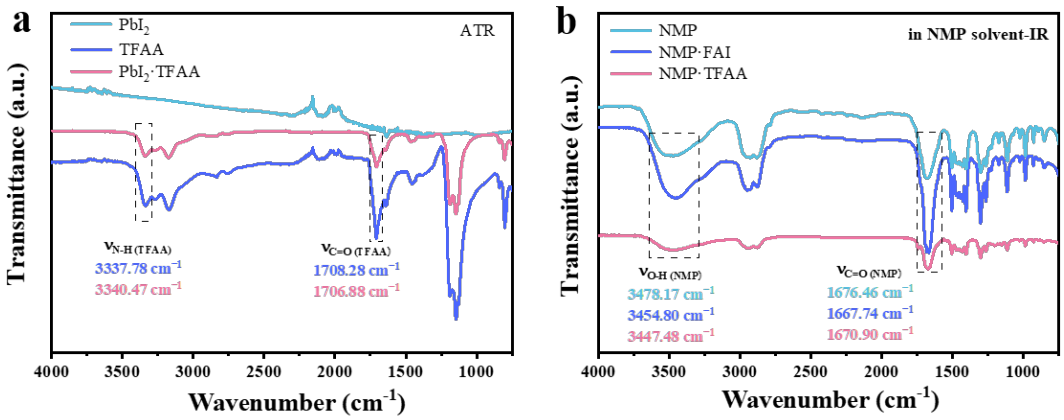

Fig. S21. ATR and IR spectra show the interaction between TFAA and the component of perovskite. FTIR spectra of a) PbI_2, TFAA, and PbI_2+TFAA, b) NMP, NMP+FAI, and NMP+TFAA. The peak of the functional group will shift to lower wavenumber position after the formation of hydrogen bonds. Additionally, the changes in peak intensity indicate strong hydrogen bonding between FAI and NMP, while NMP and TFAA exhibit weak hydrogen bonding.

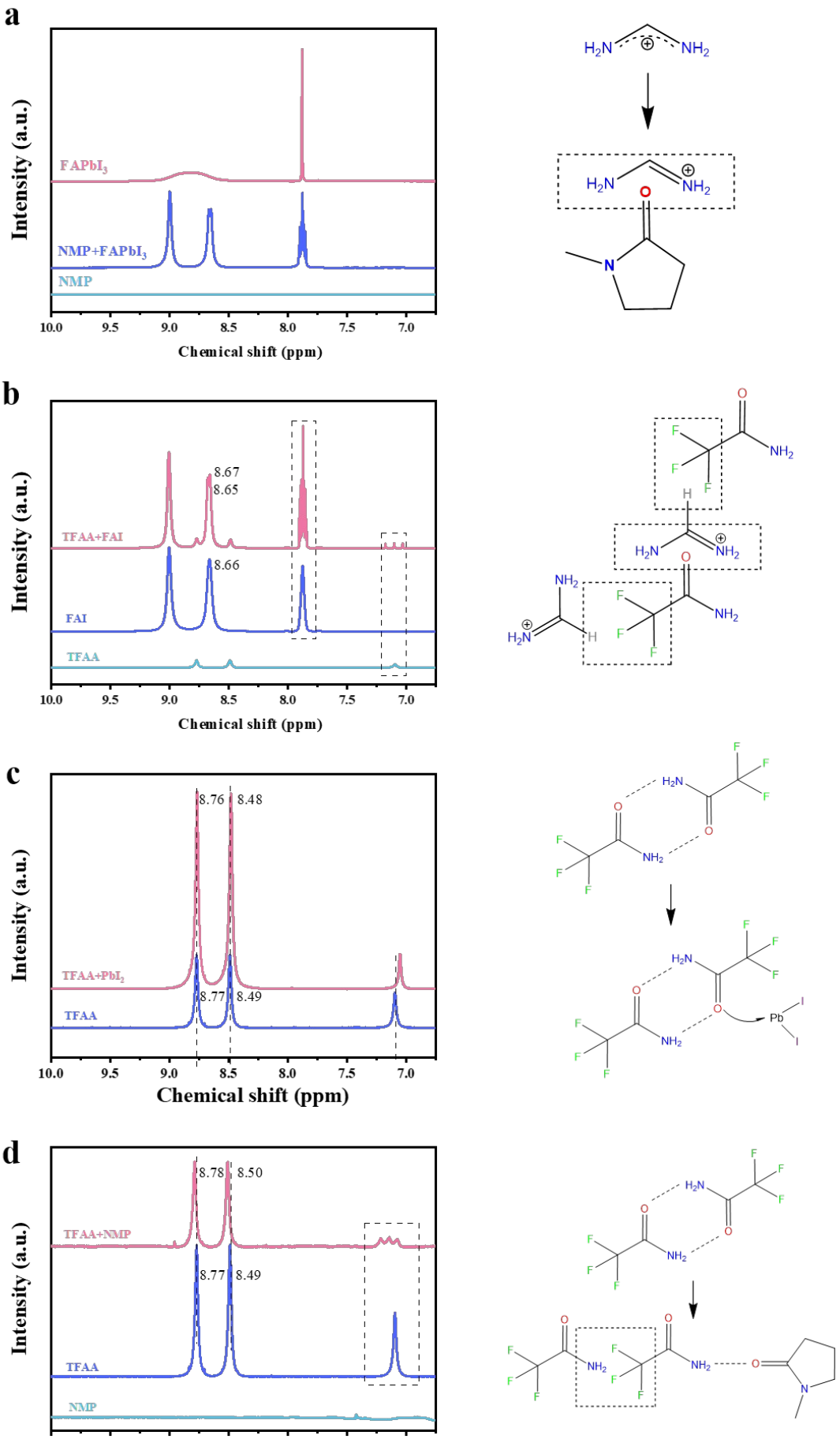
a
Intensity (a.u.)
FAPbI3
NMP+FAPbI3
NMP
10.0
9.5
9.0
8.5
8.0
7.5
7.0
Chemical shift (ppm)
b
Intensity (a.u.)
8.67
8.65
TFAA+FAI
8.66
FAI
TFAA
Chemical shift (ppm)
c
Intensity (a.u.)
8.76
8.48
TFAA+PbI2
8.77
8.49
TFAA
Chemical shift (ppm)
d
Intensity (a.u.)
8.78
8.50
TFAA+NMP
8.77
8.49
TFAA
NMP
Chemical shift (ppm)

Fig. S22. Investigation of interactions between TFAA and component of perovskite. ^{1}H NMR spectra of a) $FAPbI_3$, NMP, and NMP+$FAPbI_3$, b) FAI, TFAA, and FAI+TFAA, c) TFAA and TFAA+PbI_2, d) NMP, TFAA, and NMP+TFAA. After the formation of the majority of hydrogen bonds, the electron cloud density of hydrogen will decrease, and the chemical shift will move towards a low-field, exhibiting a significant de-shielding effect.

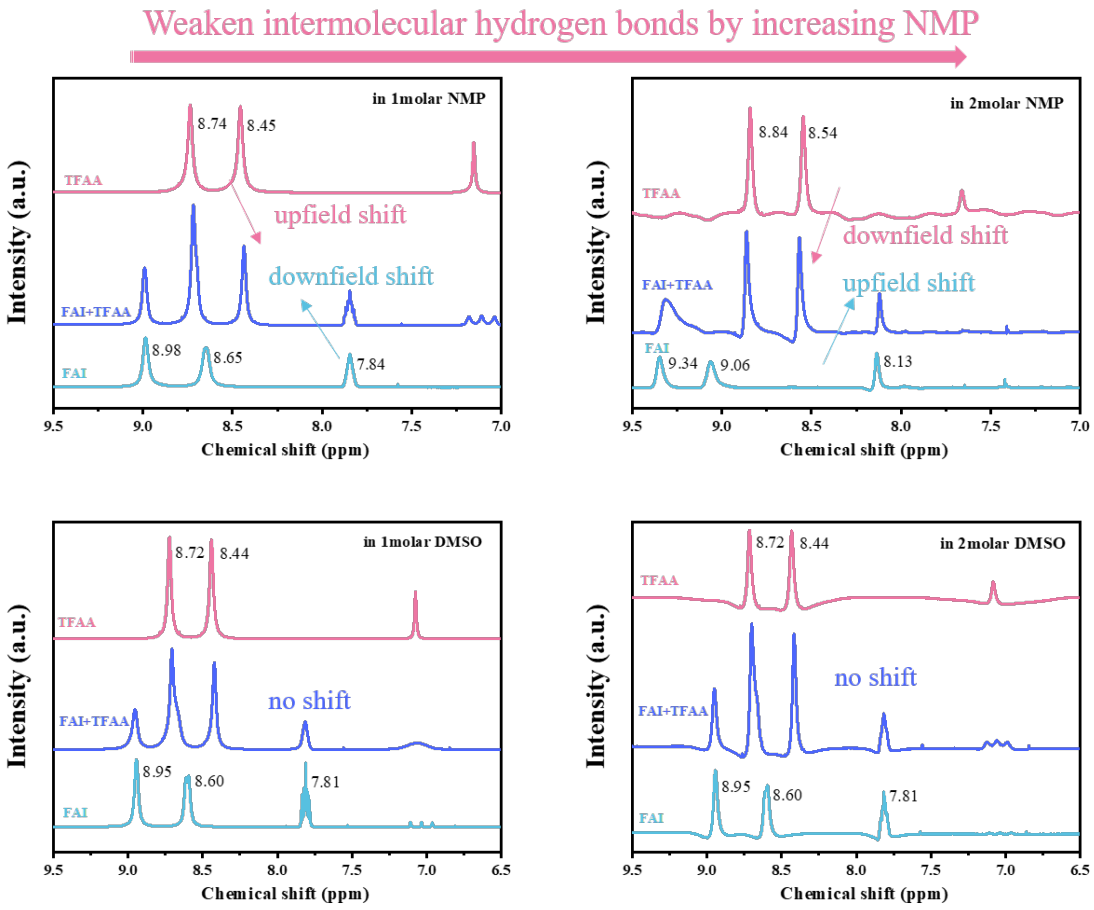

Fig. S23. Investigation of interactions among FAI, TFAA and FAI+TFAA with 1H NMR spectra. There is a complex hydrogen bonding network among FAI, TFAA, and NMP, which can not be seen in DMSO.

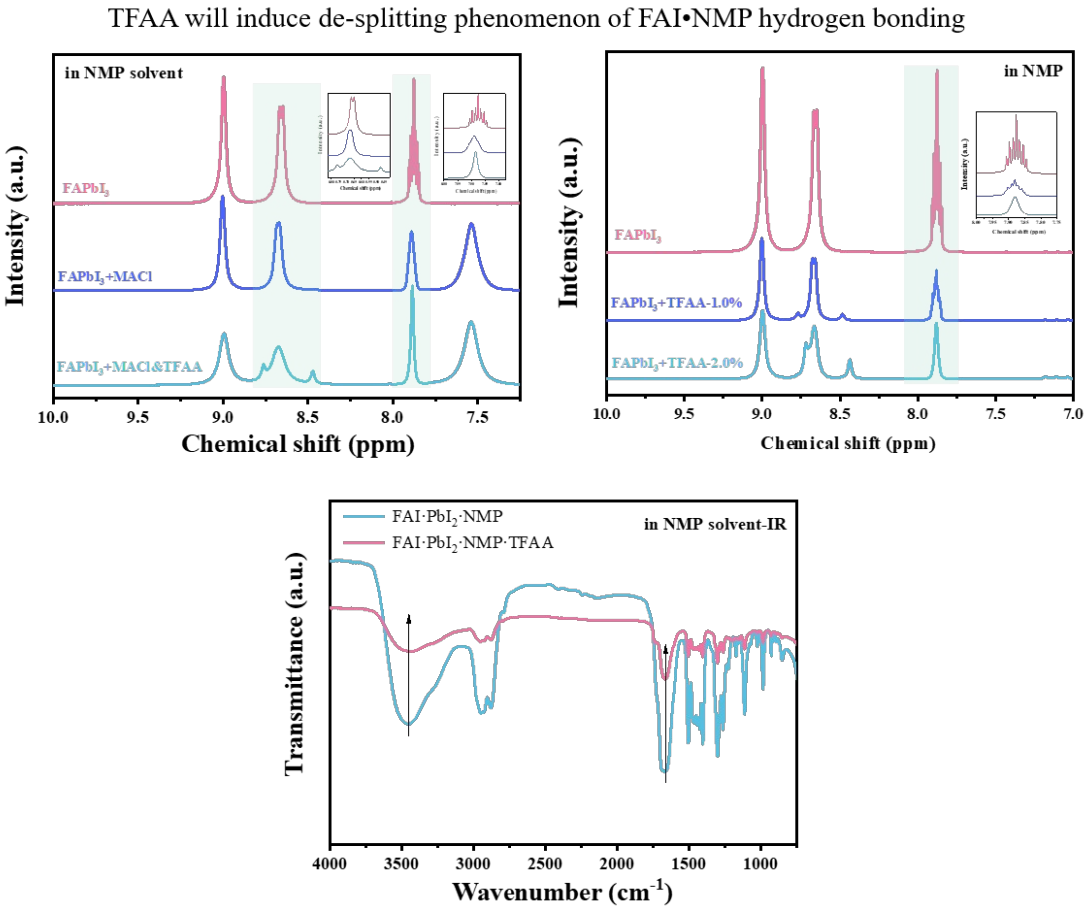

Fig. S24. Investigation of mechanism of TFAA replacing NMP by ^{1}H NMR spectra and FTIR spectra. The de-splitting phenomenon induced by the additives in the NMP solution implies the formation of perovskite species, thus greatly attenuating the presence of the solvent's intermediate phase.

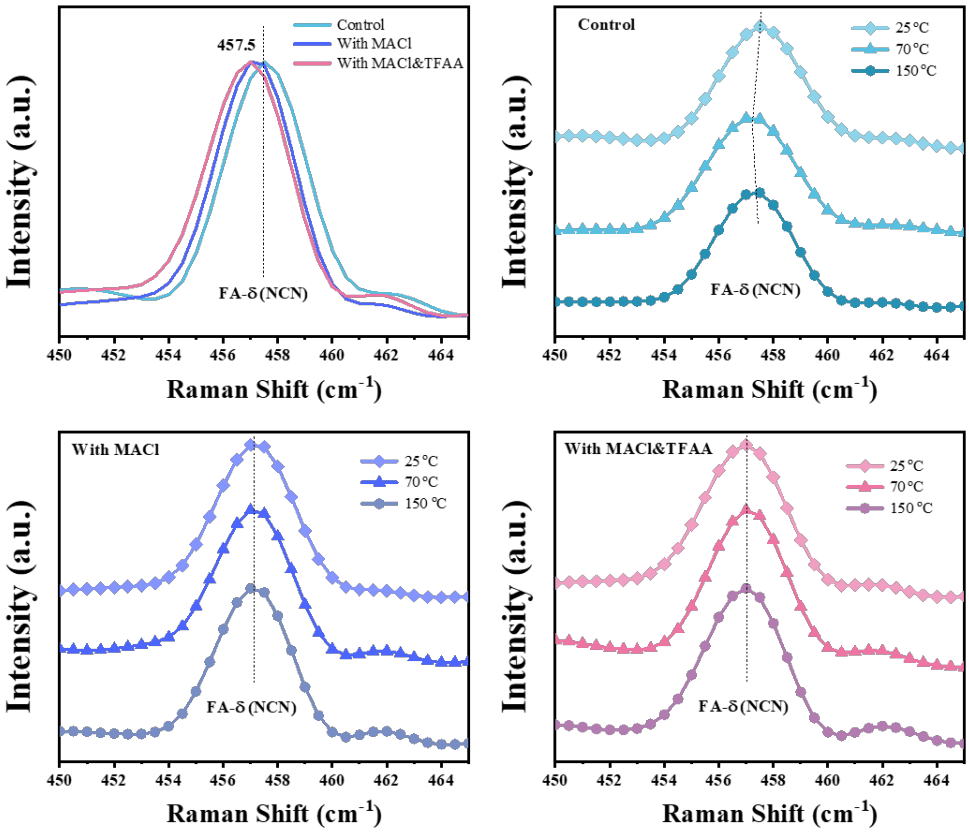

Fig. S25. Raman spectra of $FAPbI_3$ films in different conditions and Raman spectra with different temperature of films. FA-δ(NCN) stands for FA^+ bending [9]. The Raman peak shifting to lower wavenumber indicates the release of lattice distortion, while the unchanged peak positions at different temperatures suggest the assistance of the additives.

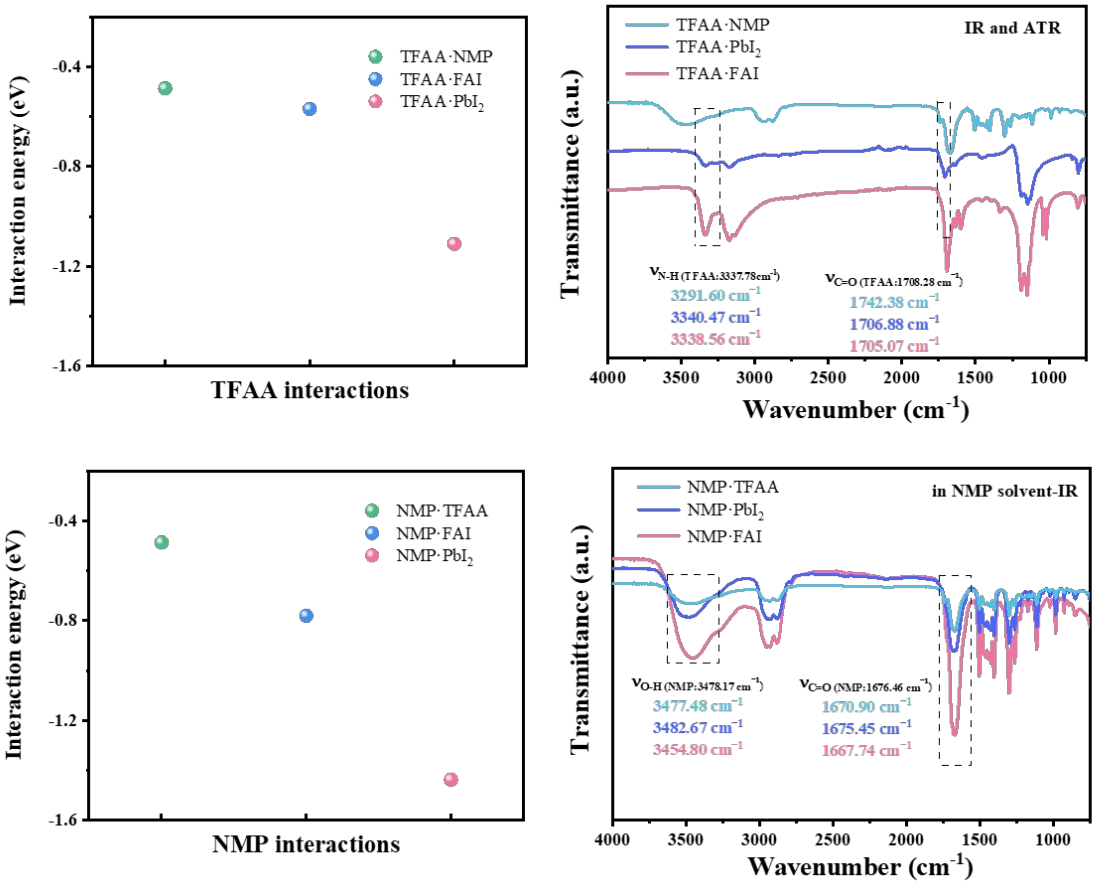

Fig. S26. Trimolecular interaction energies that comparing TFAA with NMP, and the corresponding FTIR spectra. The bonding pattern between NMP and TFAA resembles that shown in the Fig. 4c and Fig. S25-S26.

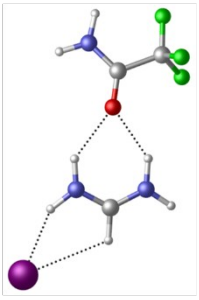

FAI·TFAA
–0.569 eV

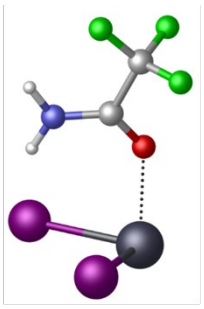

PbI_2·TFAA
–1.110 eV

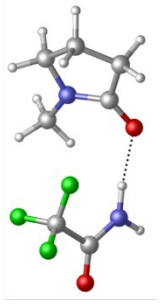

NMP·TFAA
–0.487 eV

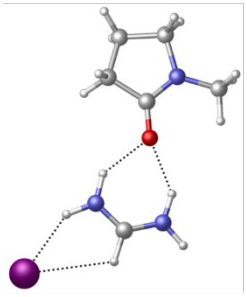

FAI·NMP
–0.780 eV

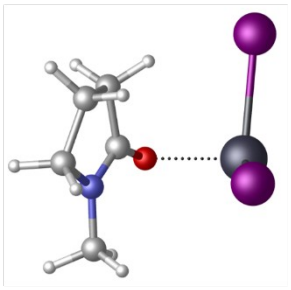

PbI_2·NMP
–1.437 eV

Fig. S27. Bimolecular structures and corresponding interaction energies resulting from DFT calculations.

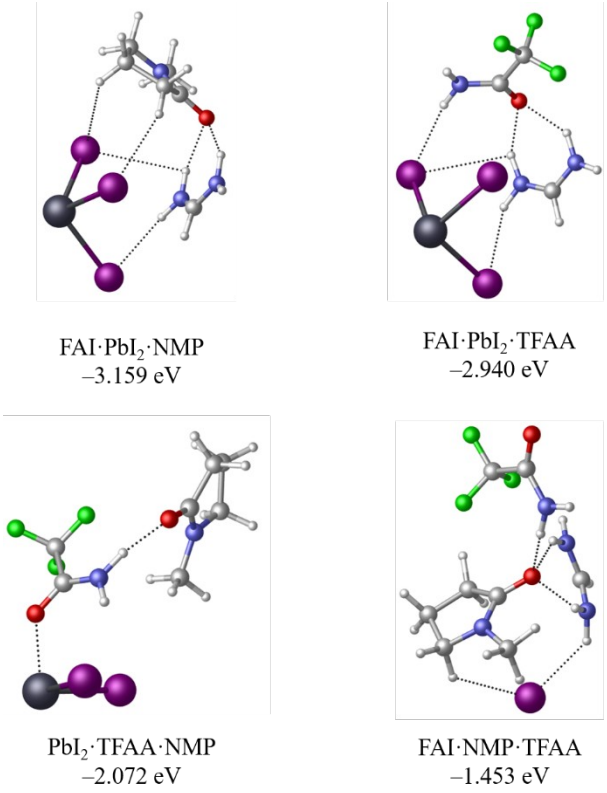

Fig. S28. Trimolecular structures and corresponding interaction energies resulting from DFT calculations.

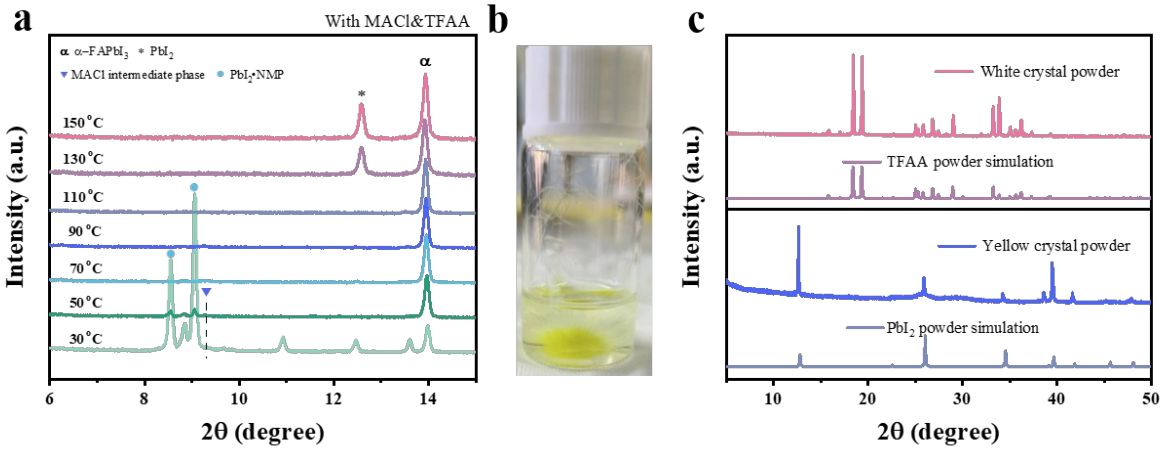

Fig. S29. a) XRD patterns of the target perovskite films annealed at different temperatures for 2 min in air. b) Photographs of PbI_2-TFAA mixed crystals and c) XRD pattern of crystal powders from Fig. S28b. XRD analysis did not reveal any new intermediate phases, indicating that TFAA, like CsI, surrounds the formed intermediates, with FAI and MACl

being incorporated into the perovskite structure first, followed by the simultaneous departure of MACl and TFAA in the subsequent process. This also explains why the strong dipolar effect of TFAA does not introduce additional compressive strain, unlike MACl, which operates at grain boundaries, rather than penetrating the lattice framework as MACl does. Another point of consideration is that the intermediate species formed by TFAA, similar to FAI•PbI_2•NMP, rapidly converts to the α-phase perovskite, making it challenging to detect.

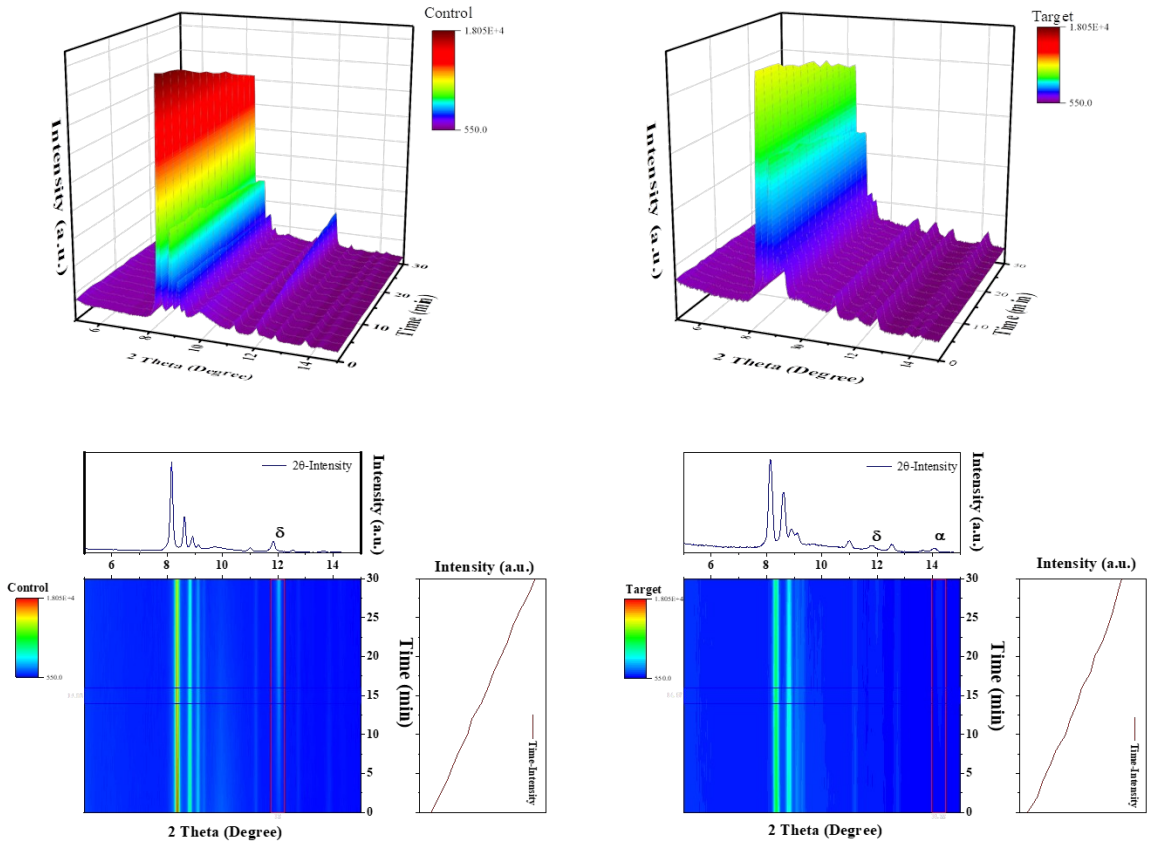

Fig. S30. In-situ XRD 3D profile and its 2D correlation mapping for $FA_{0.85}Cs_{0.15}$-perovskite films in the same control and target conditions. The perovskite films naturally dried after spinning on the ITO/SnO_2 substrates. The binary additives are also suitable for lower-FA content FA-based perovskite film.

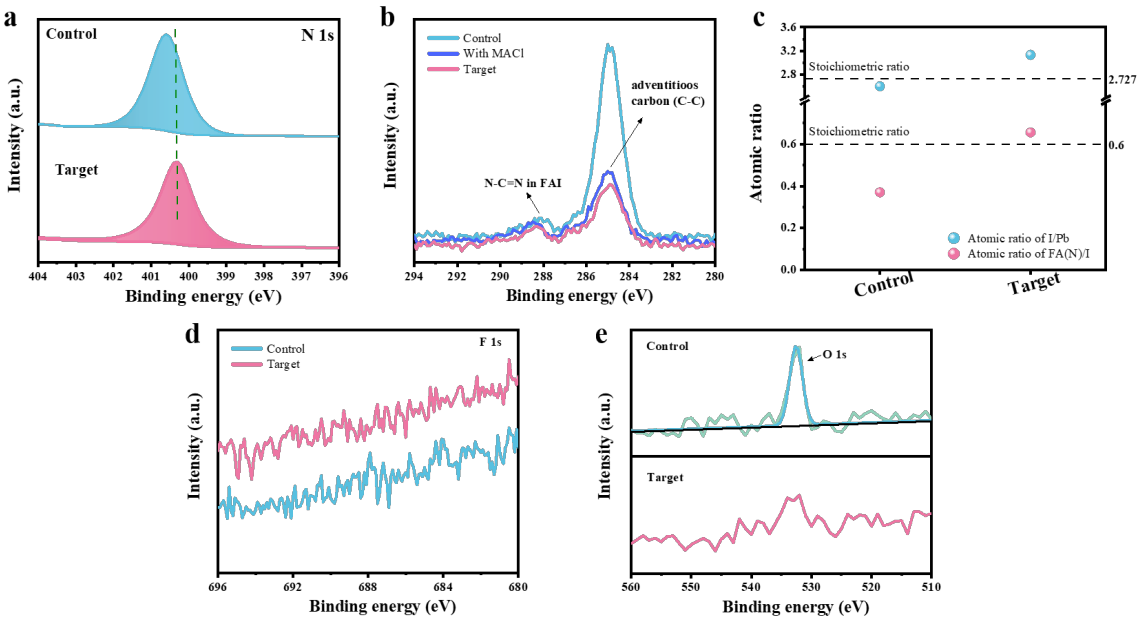

Fig. S31. XPS spectra of the core level a) N1s, b) C1s, d) F1s and e) O1s of the control and target film, respectively. c) Calculated results of I/Pb and FA(N)/I ratios from XPS test. The control film exhibits significantly lower I/Pb and FA(N)/I ratios compared to stoichiometry, likely due to surface voids. The electronic structure of perovskites with binary additives is evaluated by considering V_I-mediated trapping states on the surface. Due to the departure of the TFAA from the film, the F signal cannot be detected [10]. The lower oxygen peak intensity of O1s also confirmed that binary additives-passivation suppressed the water molecules degradation of perovskite [11].

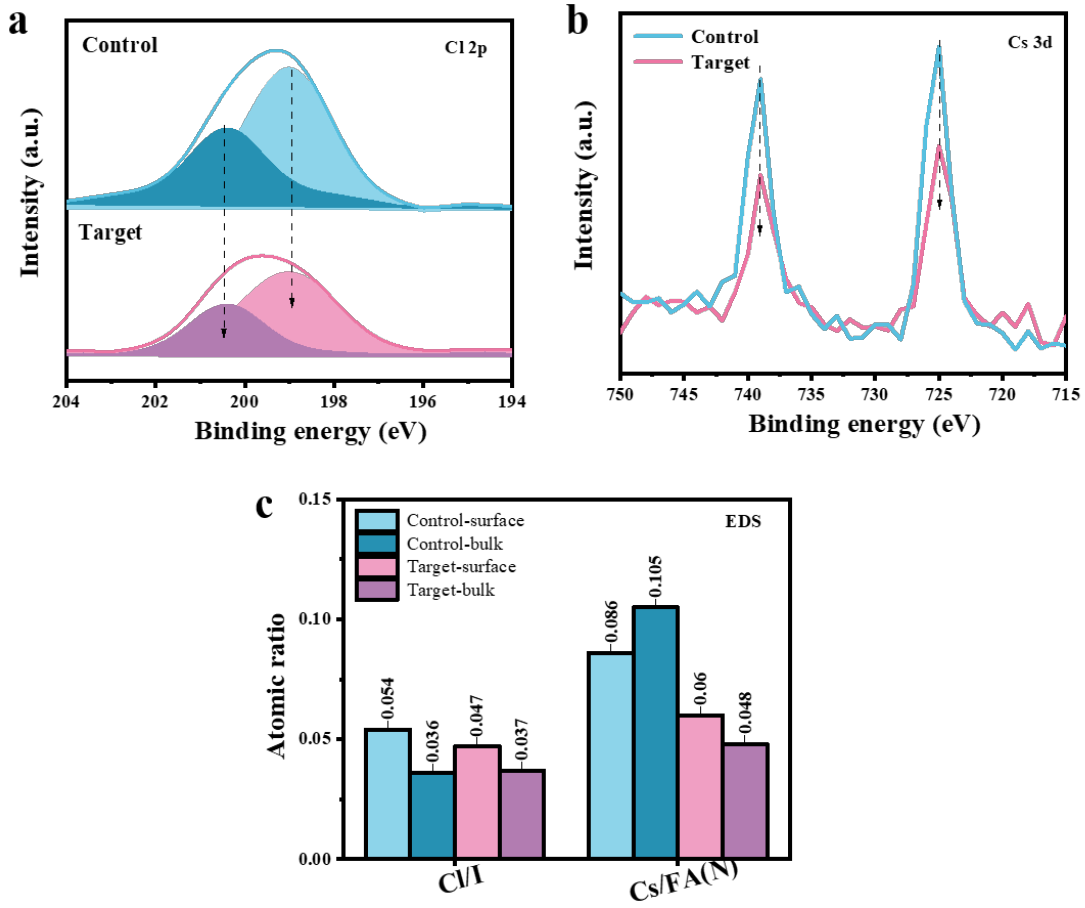

Fig. S32. a-b) XPS spectra of the core level Cl 2p and Cs 3d of the control and target film, with histograms of elemental content and atomic ratio obtained from XPS, respectively. c) Histograms of surface/bulk atomic ratio obtained from energy-dispersive spectroscopy (EDS) measurements. The target film compositions are uniformly distributed in both the surface and bulk, minimizing enrichment on the surface and potential point defects like V_{FA}, V_{Pb}, and V_I vacancies [12]. This is exemplified by the changes in Cl^- and Cs^+ ions. The decrease in Cl content on the surface indicates that Ostwald ripening during the post-treatment process inhibits excess PbI_2 formation from $PbCl_2$ exchange, as discussed earlier. The reduced Cs content on the surface is indicative of uniform distribution throughout the film, along with FA, effectively lowers the V_{FA}-induced defect concentration and thereby enhances carrier transfer and device performance.

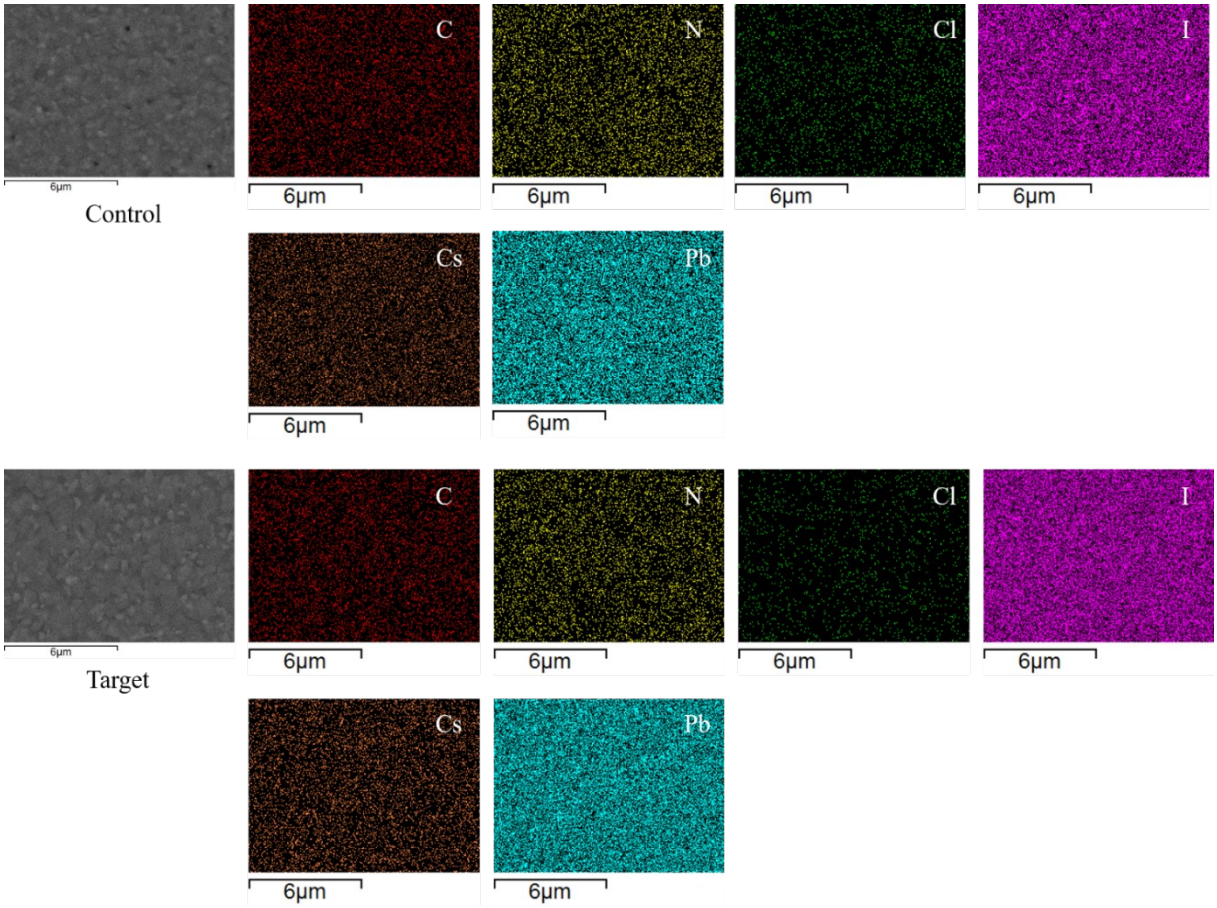

Fig. S33. Element distribution maps on surface of the control and target perovskite films by EDS measurement.

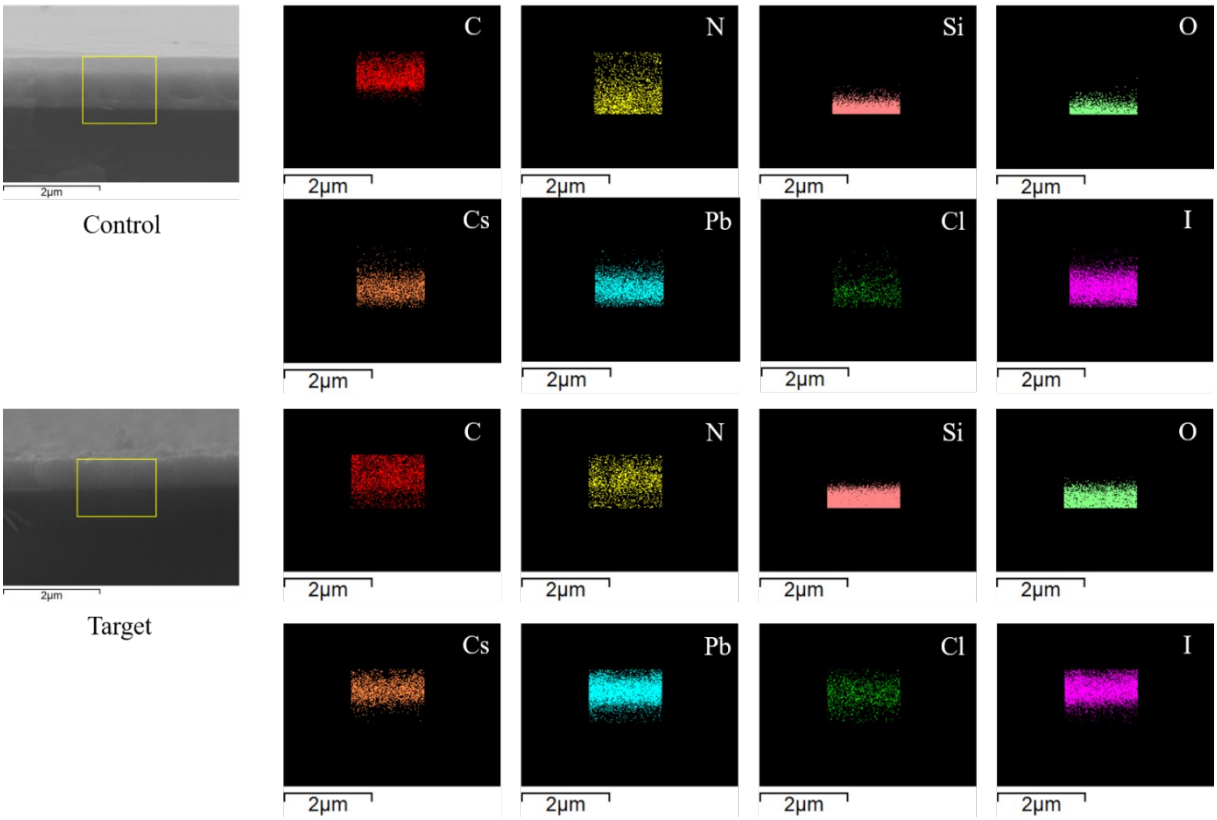

Fig. S34. Element distribution maps on bulk of the control and target perovskite films by EDS measurement.

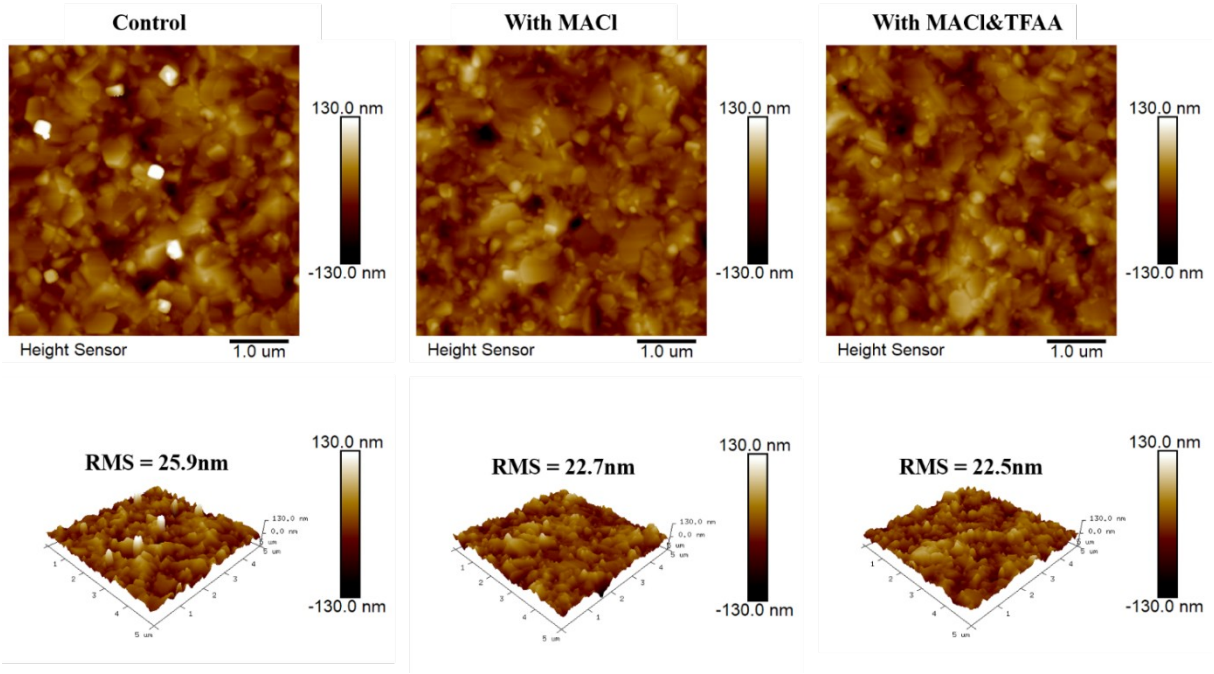

Fig. S35. Topography and three-dimensional atomic force microscopy (AFM) images of different perovskite films taken from 5x5 μm^2 area.

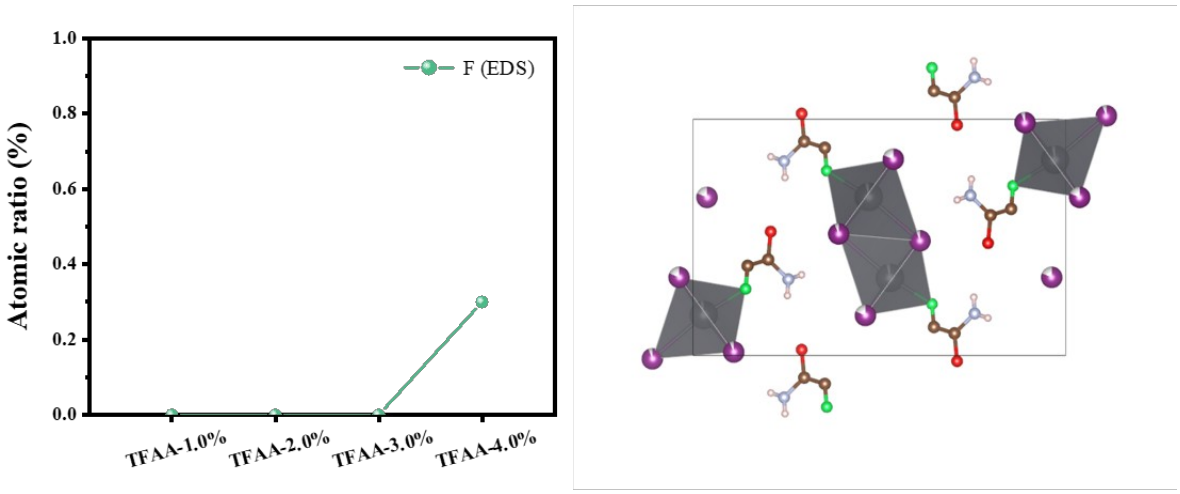

Fig. S36. The atomic ratio of F in films by EDS and the possible PbI_2•FAA (fluoroacetamide) structures. Excessive TFAA may remain in the perovskite and may lead to unexpected structural outcomes.

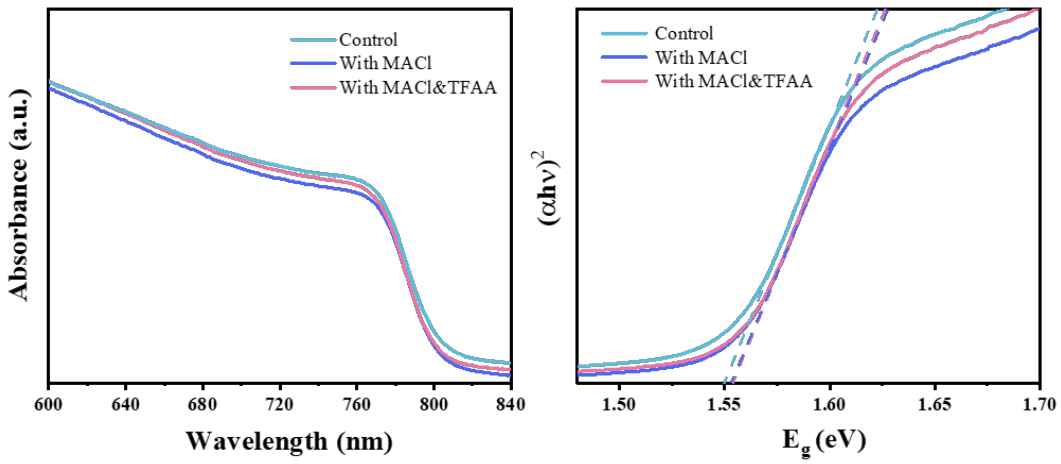

Fig. S37. UV-Vis spectra of different perovskite films and Tauc plots from UV-Vis spectra.

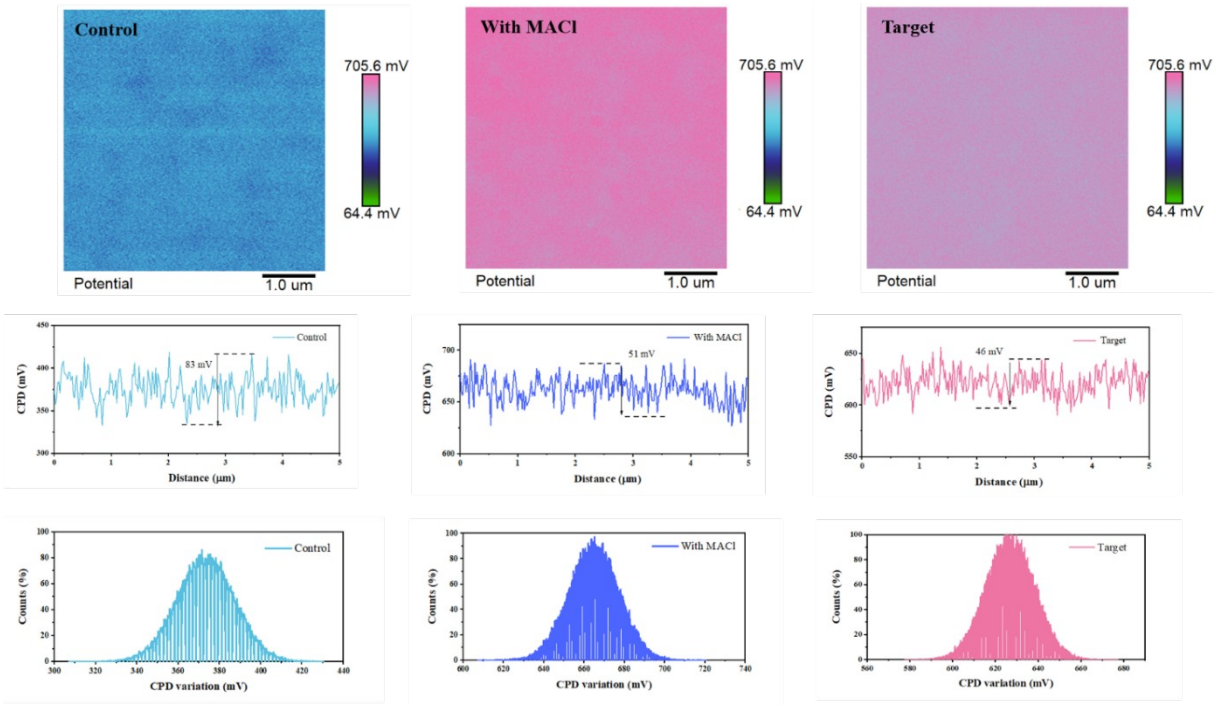

Fig. S38. KPFM measurements, the CPD line-scan spectra (5.0 μm × 5.0 μm) and CPD variation of the control, with MACl and target films. Local grain boundaries are expected to trap free carriers, leading to a decrease in the surface potential of perovskites [13]. This leads to a relatively high CPD gap (ΔCPD) between grain boundaries and adjacent grains. With the addition of binary additives, the ΔCPD between the GBs and adjacent grains decreased from 83 to 46 mV. This decrease can be related to the defect-healing properties in grain boundaries by controlling the crystallization process.

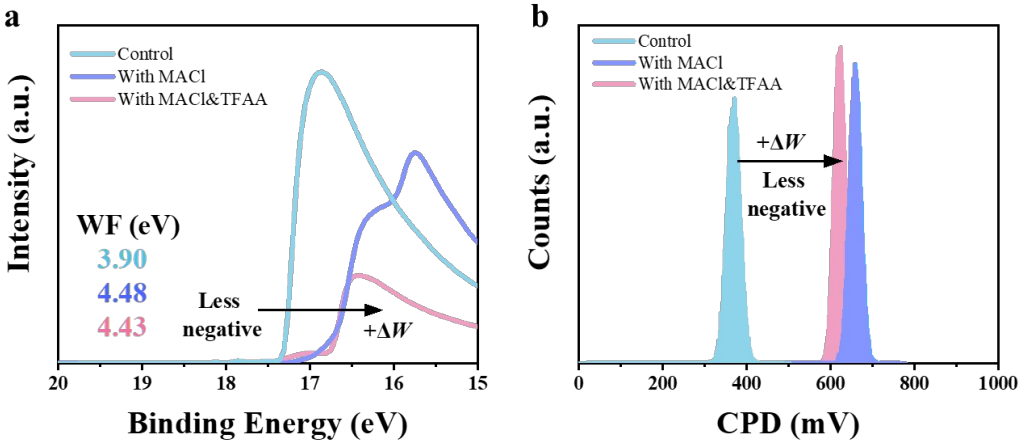

Fig. S39. a) Cut-off edge extracted from the UPS data and b) CPD distributions measured by KPFM for the different perovskite films.

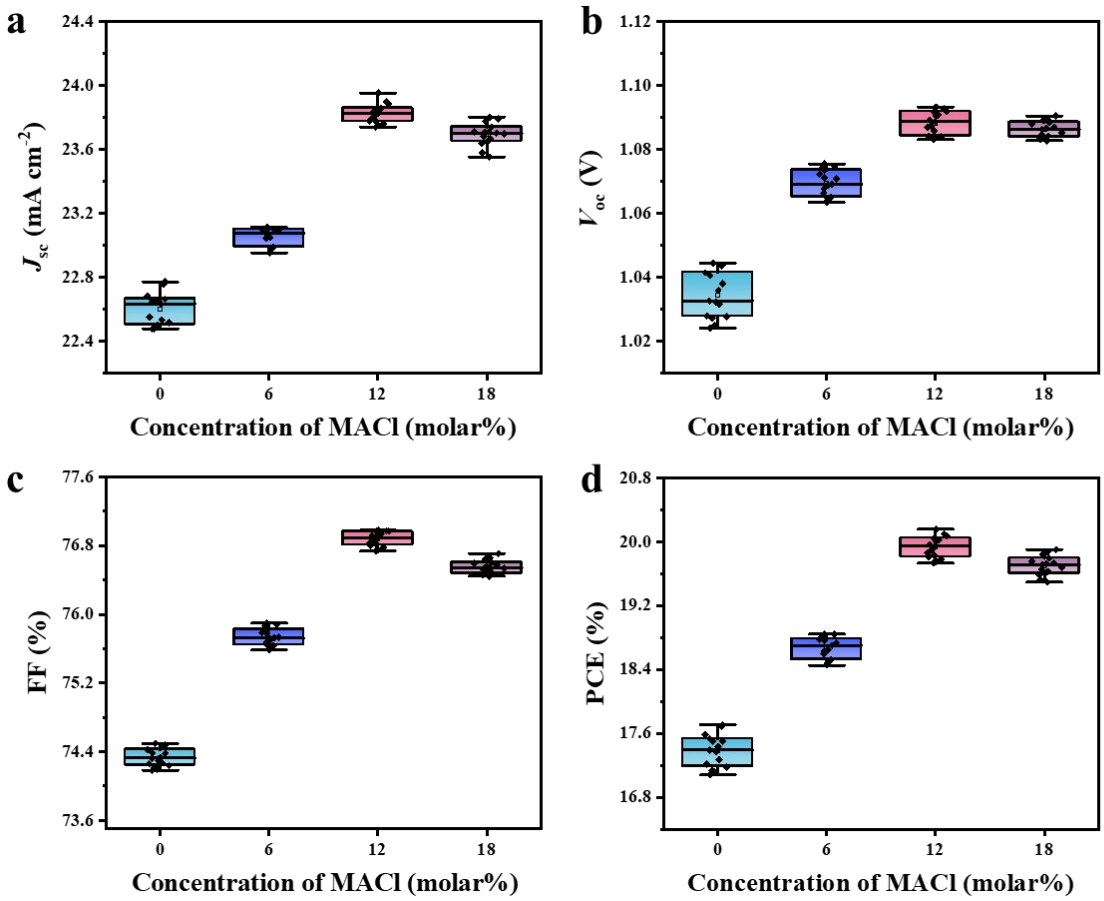

Fig. S40. Box charts of a) J_{SC}, b) V_{OC}, c) FF, and d) PCE of 15 PSCs with different concentrations of MACl modification, respectively.

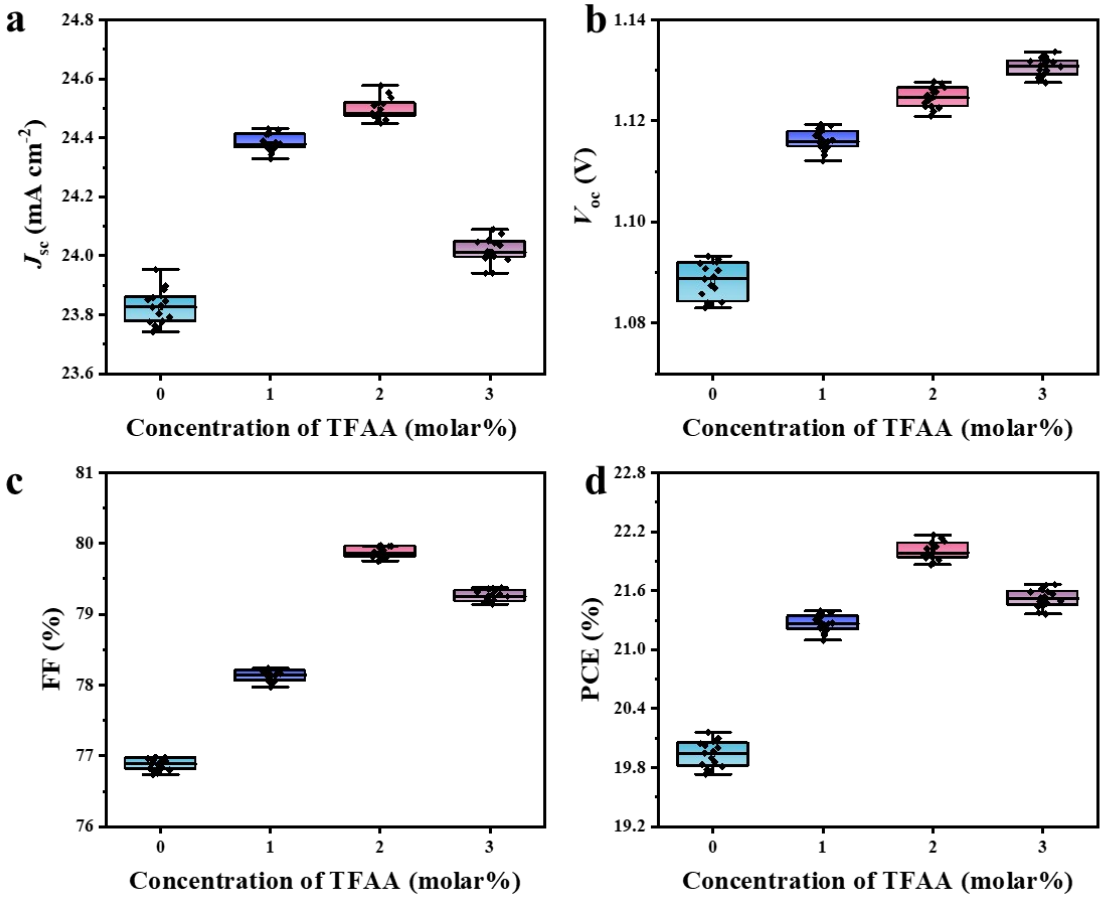

Fig. S41. Box charts of a) J_{SC}, b) V_{OC}, c) FF, and d) PCE of 15 PSCs with different concentrations of TFAA modification, respectively.

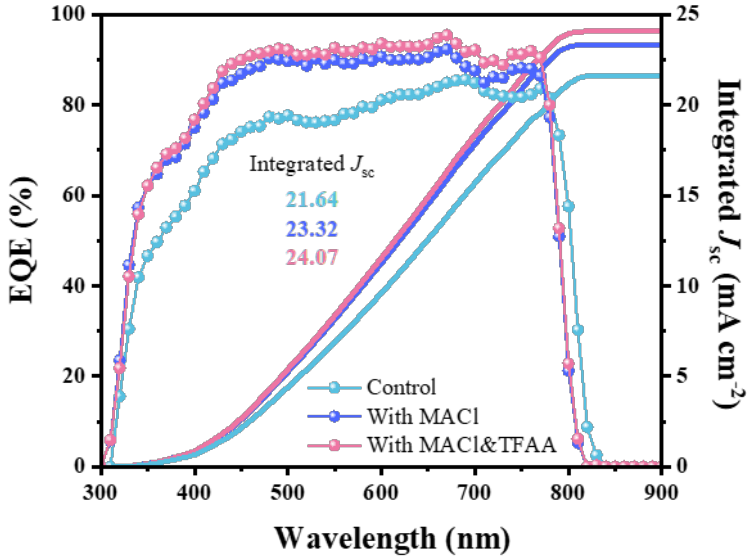

Fig. S42. External quantum efficiency (EQE) spectrum of the perovskite solar cells.

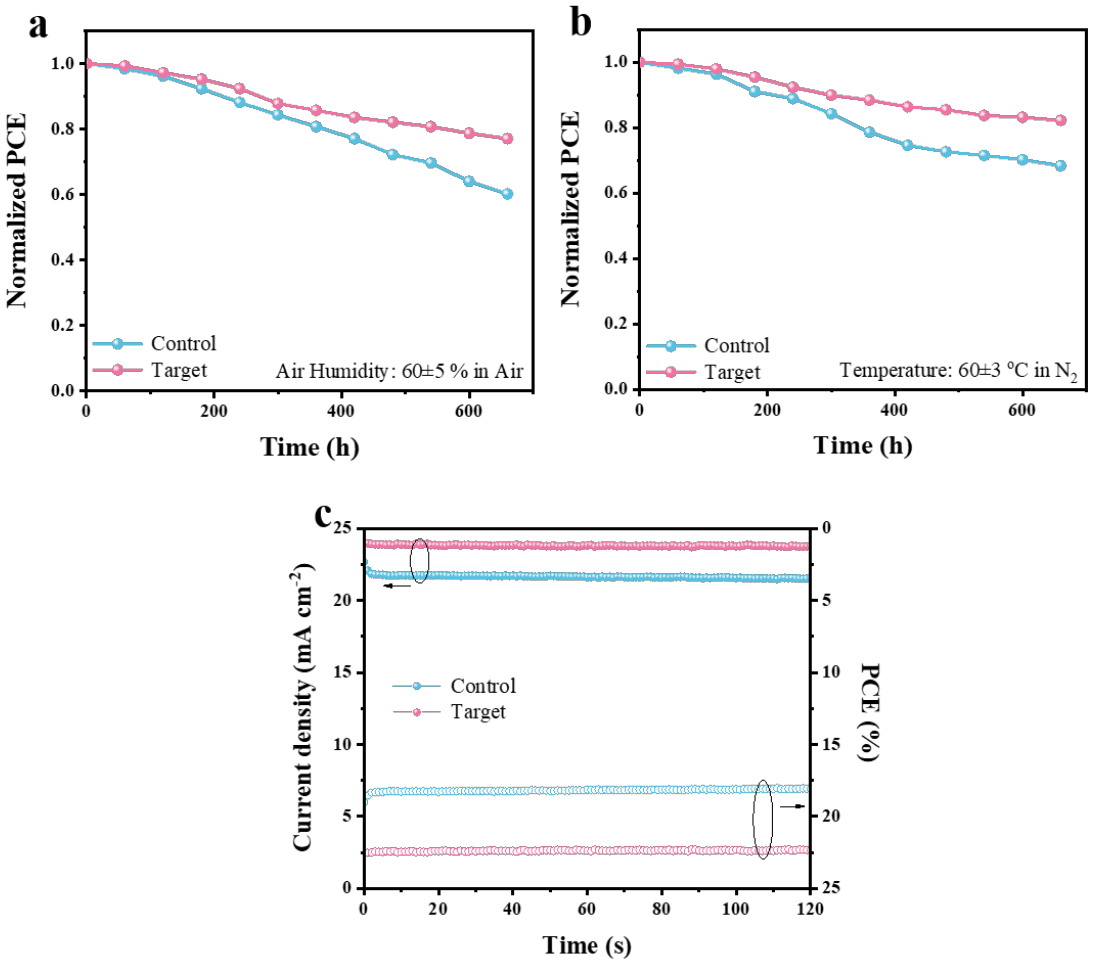

Fig. S43. a) Humidity stability test of unencapsulated devices in air with a relative humidity range of 60±5 %. b) Thermal stability test of unencapsulated devices at 60±3 °C in a N_2-filled glovebox. c) The corresponding steady-state output current density under maximum power point.

Table S1. Roles of intermediate phases in two classifications of intermediate phase engineering (IPE) and film-processing techniques with or without antisolvent.

Intermediate phase engineering	Film-processing techniques	Roles of intermediate phases
FAI•PbI_2-solvent	one-step method with antisolvent	promoting the transformation of FAI •PbI_2 into perovskite phase
FAI•MACl•PbI_2-NMP/ TFAA	one-step method wituout antisolvent binary additives: MACl TFAA	changing the perovskite crystal growth process for uniform perovskite films; promoting the formation of pure black perovskite phases; modulation of perovskite intermediate phase

Table S2. Calculated interaction energies using density functional theory (DFT) calculation [14].

Molecules	Interaction Energy (eV)
TFAA·NMP	-0.487
TFAA·FAI	-0.569
NMP·FAI	-0.780
TFAA·PbI_2	-1.110
NMP·PbI_2	-1.437
TFAA·NMP·FAI	-1.453
TFAA·NMP·PbI_2	-2.072
TFAA·FAI·PbI_2	-2.940
NMP·FAI·PbI_2	-3.159

Table S3. Fitted TRPL parameters of perovskite films in different conditions.

Sample	A_1 (%)	τ_1 (ns)	A_2 (%)	τ_2 (ns)	τ_{avg} (ns)
Control	23.62	50.00	76.37	260.01	248.22
With MACl	13.24	50.00	86.75	279.97	273.86
With MACl&TFAA	3.13	49.99	96.86	399.98	398.57

Table S4. Detailed photovoltaic parameters of different condition PSCs based on champion devices.

Sample	Direction	V_{oc} (V)	J_{sc} (mA/cm^2)	FF (%)	PCE (%)	Hysteresis
Control	Forward	1.044	22.65	73.08	17.28	0.0226
	Reverse	1.053	22.47	74.64	17.67	
With MACl	Forward	1.103	23.71	76.74	20.07	0.0179
	Reverse	1.105	23.99	77.02	20.43	
With MACl&TFAA	Forward	1.133	24.51	79.16	22.00	0.0172
	Reverse	1.136	24.51	80.34	22.38	

Note: the active area of each device is 0.04 cm^2.

Table S5. Average photovoltaic parameters of antisolvent-free PSCs prepared with different concentrations of MACl.

Concentration (mol%)	V_{oc} (V)	J_{sc} (mA/cm^2)	FF (%)	PCE (%)
0%	1.034±0.01	22.63±0.15	74.34±0.15	17.30±0.42
6%	1.069±0.06	23.04±0.09	75.74±0.15	18.65±0.39
12%	1.088±0.05	23.85±0.10	76.86±0.12	19.94±0.21
18%	1.087±0.04	23.68±0.13	76.58±0.13	19.70±0.20

Note: the average parameters are calculated from 15 devices.

Table S6. Average photovoltaic parameters of antisolvent-free PSCs prepared with different concentrations of TFAA.

Concentration (mol%)	V_{oc} (V)	J_{sc} (mA/cm^2)	FF (%)	PCE (%)
0%	1.088±0.05	23.85±0.10	76.86±0.12	19.94±0.21
1%	1.116±0.04	24.38±0.05	77.97±0.13	21.24±0.15
2%	1.124±0.03	24.51±0.06	79.86±0.11	22.01±0.15
3%	1.131±0.06	24.01±0.07	79.25±0.12	21.51±0.15

Note: the average parameters are calculated from 15 devices.

Table S7. Elemental content analysis for perovskite film in different conditions by XPS measurements.

XPS (surface)	Stoichiometric ratio	Control	Target
N1s	29.03	17.52	28.31
Cs3d	1.62	5.46	4.23
Pb4f	17.74	18.20	13.78
Cl2p	3.23	12.62	10.51
I3d	48.39	47.29	43.16
Total (%)	100	100	100
Atomic ratio of I/Pb	2.727	2.598	3.13
Atomic ratio of FA(N)/I	0.600	0.370	0.656
Atomic ratio of Cs/FA(N)	0.056	0.312	0.149
Atomic ratio of Cl/I	0.067	0.253	0.243

Table S8. Elemental content analysis for perovskite film in different conditions by EDS measurements.

EDS	Stoichiometric ratio	Control surface	Control bulk	Target surface	Target bulk
FA(N)	29.03	32.21	36.31	42.24	42.28
Cs	1.62	2.78	3.80	2.52	2.01
Pb	17.74	16.16	16.92	13.10	14.35
Cl	3.23	2.48	1.48	1.90	1.47
I	48.39	46.37	40.81	40.24	39.89
Total (%)	100	100	100	100	100
Atomic ratio of Cs/FA(N)	0.056	0.086	0.105	0.060	0.048
Atomic ratio of Cl/I	0.067	0.054	0.036	0.047	0.037

References

[1] Y. Zhang, S.-G. Kim, D. Lee, H. Shin, N.-G. Park, Energy Environ. Sci. 12 (2019) 308-321, https://doi.org/10.1039/C8EE02730G.

[2] J.-D. Chai, M. Head-Gordon, Phys. Chem. Chem. Phys. 10 (2008) 6615-6620, https://doi.org/10.1039/B810189B.

[3] A.D. McLean, G.S. Chandler, J. Chem. Phys. 72 (2008) 5639-5648, https://doi.org/10.1063/1.438980.

[4] G.W. Spitznagel, T. Clark, P. von Ragué Schleyer, W.J. Hehre, J Comput Chem 8 (1987) 1109-1116, https://doi.org/10.1002/jcc.540080807.

[5] M.J. Frisch, J.A. Pople, J.S. Binkley, J. Chem. Phys. 80 (1984) 3265-3269, https://doi.org/10.1063/1.447079.

[6] W.R. Wadt, P.J. Hay, J. Chem. Phys. 82 (1985) 284-298, https://doi.org/10.1063/1.448800.

[7] G.W.T. M. J. Frisch, H. B. Schlegel, G. E. Scuseria, M. A. Robb, J. R. Cheeseman, G. Scalmani, V. Barone, G. A. Petersson, H. Nakatsuji, et al, (2016).

[8] Y. Wu, G. Xu, J. Xi, Y. Shen, X. Wu, X. Tang, J. Ding, H. Yang, Q. Cheng, Z. Chen, Y. Li, Y. Li, Joule 7 (2023) 398-415, https://doi.org/10.1016/j.joule.2022.12.013.

[9] S. Ruan, D.P. McMeekin, R. Fan, N.A.S. Webster, H. Ebendorff-Heidepriem, Y.-B. Cheng, J. Lu, Y. Ruan, C.R. McNeill, J. Phys. Chem. C 124 (2020) 2265-2272, https://doi.org/10.1021/acs.jpcc.9b08917.

[10] H. Zhang, W. Xiang, X. Zuo, X. Gu, S. Zhang, Y. Du, Z. Wang, Y. Liu, H. Wu, P. Wang, Q. Cui, H. Su, Q. Tian, S. Liu, Angew Chem Int Ed Engl 62 (2023) e202216634, https://doi.org/10.1002/anie.202216634.

[11] L. Yuan, J. Wang, P. Huang, Q. Yin, S. Zou, L. Wang, Z. Zhang, H. Luo, F. Liu, J. Qiu, J. Xie, L. Ding, K. Yan, Small Methods 7 (2023) 2201467, https://doi.org/10.1002/smtd.202201467.

[12] L. Fu, H. Li, L. Wang, R. Yin, B. Li, L. Yin, Energy Environ. Sci. 13 (2020) 4017-4056, https://doi.org/10.1039/D0EE01767A.

[13] J. Zhang, X. Jiang, X. Liu, X. Guo, C. Li, Adv. Funct. Mater. 32 (2022) 2204642, https://doi.org/10.1002/adfm.202204642.

[14] J.-W. Lee, Z. Dai, C. Lee, H.M. Lee, T.-H. Han, N. De Marco, O. Lin, C.S. Choi, B. Dunn, J. Koh, D. Di Carlo, J.H. Ko, H.D. Maynard, Y. Yang, J. Am. Chem. Soc. 140 (2018) 6317-6324, https://doi.org/10.1021/jacs.8b01037.